2016

Band gap study of lead chalcogenide alloys

Vaughan Patterson
University of Wollongong

Band Gap Study of Lead Chalcogenide Alloys

A thesis completed as an important part of a postgraduate student's exposure to advanced experimental techniques and the scientific approach to research.

Submitted in fulfilment of the requirements for the award of the degree

MASTER OF PHILOSOPHY (MATERIALS ENGINEERING)

From

UNIVERSITY OF WOLLONGONG (UOW)

By

VAUGHAN PATTERSON

AUSTRALIAN INSTITUTE FOR INNOVATIVE MATERIALS (AIIM)

2016

CERTIFICATION

I, Vaughan Lochinvar Patterson, declare that this thesis, submitted in fulfilment of the requirements for the award of Master of Philosophy, in the Faculty of Engineering and Information Sciences, University of Wollongong, is completely my own work unless otherwise referenced or acknowledged. This document has not been submitted for qualifications at any other academic institution.

(Signature) Vaughan L. Patterson

29 August 2016

Acknowledgements

First I would like to thank my supervisor and mentor Dr. Sima Aminorroaya. During the completion of this course Dr. Sima Aminorroaya has supported me enormously in preparation of this Thesis and been available for consultation under any circumstances. She has not only been very patient and encouraging throughout this process, but also been very honest and not held back in her expectations of me. Dr. Aminorroaya has challenged me to explore further into the experimental techniques and procedures undertaken which I will be forever grateful, as I have never been exposed to such raw passion for pushing boundaries in materials. I can honestly say she has changed my whole perspective on scientific research and I would never have completed this Thesis without her unwavering guidance.

I would also like to thank Rafael Santos and Andrew Manettas, because since I arrived at the Australian Institute for Innovative Materials (AIIM) they have been extremely helpful in their contribution to my thesis. This would not have been possible without their assistance in not only the experimental procedures, but in the data analysis and report writing.

Finally I would like to thank my mother, father and partner Sarah who have always believed in my academic abilities, and have provided me with the opportunities to be successful no matter what path I take or how successful I am eventually. My parents have supported me both financially and emotionally for the 24 years of my life and I will always be eternally in debt to them for their belief in me. Although it has been an intense last 6 months where my father was diagnosed with prostate cancer and my mother found new ways to injure herself, they have always found time to ask how my research was going and offer to assist in any way they can.

Abstract

Lead chalcogenides (PbQ, Q = Te, Se and S) have been applied in many devices as a result of their narrow band gaps, low electrical resistivity and high carrier mobility. The band gaps of lead chalcogenides have shown to change energy upon alloying and altering carrier concentration. This technique is known as band engineering and has been researched thoroughly as a method of improving performance in thermoelectrics, thermophotovoltaics, solar cells, UV-LEDs, laser, transistors and much more. However systematic research into the band gap energies of lead chalcogenide solid solution alloys has received little attention.

Here, the intrinsic solid solution ternary $(PbTe)_{1-x}(PbSe)_x$ and quaternary $(PbTe)_{0.9-y}(PbSe)_{0.1}(PbS)_y$ and $(PbTe)_{0.65-y}(PbSe)_{0.35}(PbS)_y$ alloys are fabricated to determine their band gap by optical absorption edge measurements using Diffuse Reflectance Infrared Fourier Transform Spectroscopy (DRIFTS). A positive band gap bowing occurs which challenges the accepted linear relationship with composition. A small band gap bowing parameter of -0.052 ± 0.011 eV was obtained for the PbS-free ternary $(PbTe)_{1-x}(PbSe)_x$ alloy as a result of the disparity in electronegativity and valence electron potential of the Te and Se atoms. A significantly larger band gap bowing of -0.21813 ± 0.01561 and -0.08326 ± 0.02352 eV was acquired for quaternary solid solution $(PbTe)_{0.9-y}(PbSe)_{0.1}(PbS)_y$ and $(PbTe)_{0.65-y}(PbSe)_{0.35}(PbS)_y$ alloys respectively. The considerably larger bowing parameter for the PbS-alloyed quaternary alloys compared to the ternary system was determined to be associated with increased mismatch of ionicity and lattice parameters. Whereas, the difference in bowing parameters between the two quaternary systems is originated from the larger miscibility gap that occurs in $(PbTe)_{0.9-y}(PbSe)_{0.1}(PbS)_y$ system compared to $(PbTe)_{0.65-y}(PbSe)_{0.35}(PbS)_y$ system.

The temperature dependent thermal conductivity of $PbSe_{0.1}Te_{0.9}$, $PbSe_{0.1}S_{0.9}$ and $PbSe_{0.35}S_{0.65}$ revealed that the contribution of thermally activated minority charge carrier in bipolar conductivity is reduced in $PbSe_{0.1}S_{0.9}$ and $PbSe_{0.35}S_{0.65}$ alloys as a result of band gap widening.

Table of Contents

List of Figures

List of Tables

List of Abbreviations

FCC	Face-Centred Cubic
XRD	X-ray Diffraction
CB	Conduction Band
VB	Valence Band
SPB	Single Parabolic Band
UV-vis	Ultraviolet Visible
FTIR	Fourier Transform Infrared
DRIFTS	Diffuse Reflectance Infrared Transform Spectroscopy
MIR	Mid Infrared Range
WAT	Weak Absorption Tail
SPS	Spark Plasma Sintering
LFA	Laser Flash Apparatus
PDOS	Partial Density of States
LSR	Linsies – Seebeck and Resistivity Unit
E_g	Band Gap
zT	Thermoelectric figure of merit
ξ	Fermi Level
S	Seebeck
σ	Electrical Conductivity
κ	Thermal Conductivity
κ_b	Bipolar Conductivity Term
L	Light Valence Band
Σ	Heavy Valence Band

ΔE	Valence Band Offset
α	Absorption Coefficient
ħω	Energy of Photon
PL	Photoluminescence
h	Planck Constant
B	Frequency Dependent Constant
λ	Wavelength
ρ	Electrical Resistivity
D_T	Thermal Diffusivity
C_p	Specific Heat Capacity
k_b	Boltzmann Constant
$\|S\|_{max}$	Maximum Absolute Seebeck
U_S	Symmetric Potential Term
U_a	Asymmetric Potential Term
$\boldsymbol{c_\tau}$	Pair Correlation Function
-eV	Valence Electron Potential
r	Ionic Radius
b	Bowing Parameter

Chapter 1

Introduction

Lead chalcogenides (PbQ, Q = Te, Se and S) are becoming increasingly popular for use in innovative devices due to their narrow band gaps and interesting electronic properties. Through investigation into the electronic band structure of semiconductors such as lead chalcogenides, it has been discovered that tuning this complicated property can lead to enhanced performance of these materials in applications such as thermoelectrics, thermophotovoltaics, solar cells, infrared lasers and detectors. What separates lead chalcogenides from other semiconductors is their unique electronic band structure that can be manipulated through alloying or impurity elements doping. The aim of this work is to determine the band gap of lead chalcogenide alloys as a function of composition. This information can lead to further advances in tuning band gap and lattice parameters for optical and electronic applications.

Here, the band gap energies of a ternary and two quaternary lead chalcogenide systems are determined by measuring the optical absorption edge via a technique known as Diffuse Reflectance Infrared Fourier Transform Spectroscopy (DRIFTS). The room temperature Seebeck coefficient and resistivity of quaternary systems as well as the thermal conductivity of some of samples were measured in order to correlate the electronic transport properties of these compounds to variations obtained in energy of band gaps as a function of composition adjustment.

The ternary system of $(PbTe)_{1-x}(PbSe)_x$ was selected to examine the effect of increased PbSe concentration on the band gap of binary PbTe. The quaternary $(PbTe)_{0.9-y}(PbSe)_{0.1}(PbS)_y$ and $(PbTe)_{0.65-y}(PbSe)_{0.35}(PbS)_y$ systems were chosen to determine how the band gap of ternary $(PbTe)_{1-x}(PbSe)_x$ alloys changes with PbS content.

Chapter 2 introduces the structure and electronic band structure including band gap energies of Pb chalcogenides and their alloys. The significance of band gap on electronic transport properties of the alloys will be discussed in details. In this chapter,

various available techniques for measuring the band gap of semiconductors will be described.

The process for fabrication of these samples and various characterization techniques, which was employed to determine their crystal structure and electronic transport properties are explained in Chapter 3. Experimental processes such as X-ray diffraction (XRD), Fourier transform infrared (FTIR) spectroscopy and laser flash apparatus (LFA) will be described in terms of sample preparation, principles of measurement and calculation of data.

The room temperature energy band gaps of ternary and quaternary Pb chalcogenides are as a function of composition is discussed in details in Chapters 4. The bowing parameter of each system is calculated and the factors affecting this parameter such as atomic size, ionicity, solubility, electronegativity and valence electron potential are discussed in details.

The electronic transport properties of some samples are explained in Chapter 5. The room temperature Seebeck coefficient and electrical resistivity of quaternary systems are discussed as a function of PbS concentration. The influence of band gap energy on bipolar effect of narrow band gap Pb chalcogenides is discussed by measured thermal conductivities of the samples. Finally the band gaps are estimated for some alloys through temperature dependent Seebeck and resistivity measurements. This data are compared to optical band gap measured for these alloys (detailed in Chapter 4).

The thesis is concluded in Chapter 6 and possible future works are outlined.

Chapter 2

Literature Review

2.1. Lead Chalcogenides

Lead chalcogenides are semiconducting compounds, which are comprised of lead combined with group VI atoms (chalcogen: Te, Se and S). The properties of all these lead chalcogenides are quite similar. These semiconductors are isomorphic in nature, similar chemical bonding, have fairly comparable production methods, contain much the same phase diagrams and most importantly are able to be extrinsically doped in the same fashion [1].

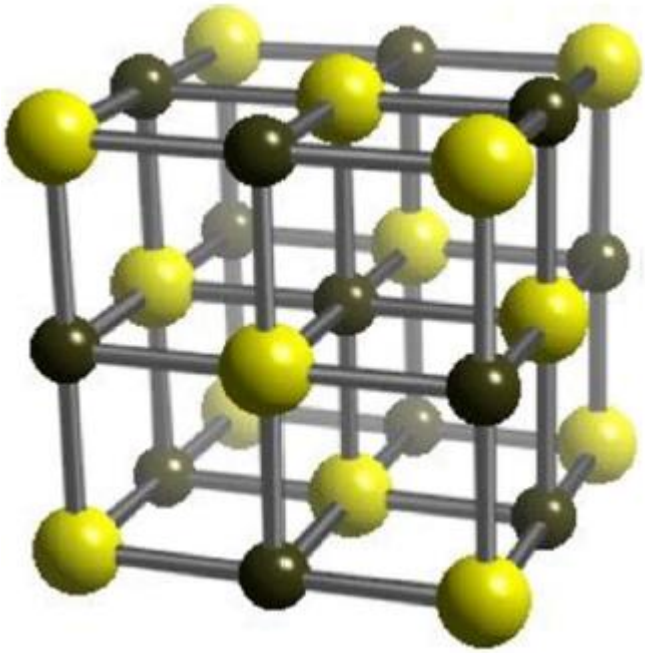

Figure 2.1: The cubic lattice structure for the lead chalcogenides PbTe, PbSe and PbS. Pb is represented by the green dots and Te/Se/S by the yellow dots [2].

Lead chalcogenides have a cubic lattice structure, with a unit cell comprised of a Face-Centered Cubic (FCC) with NaCl structure and atoms of coordination number six (Figure 2.1). Through techniques such as X-ray diffraction (XRD) it can be shown that the lattice constant and densities displays an increase in steps of approximately 10%

from lead sulfide to lead Selenide [3]. The Brillouin zone of the lead chalcogenides is displayed in Figure 2.2. At reasonably low temperatures, the lead chalcogenide crystal is quite brittle in nature and cleaves along the [100] plane with minimal force applied. There are four ellipsoids in the lead chalcogenides investigated, with the boundary edge of the Brillouin zone being the positioning of the extrema across the <111> direction [3]. All three lead chalcogenides contain energy surfaces at the boundary of the VB and CB shaped as elongated ellipsoids along this <111> direction; however the PbTe ellipsoids are much more strongly elongated compared to that of PbSe and PbS.

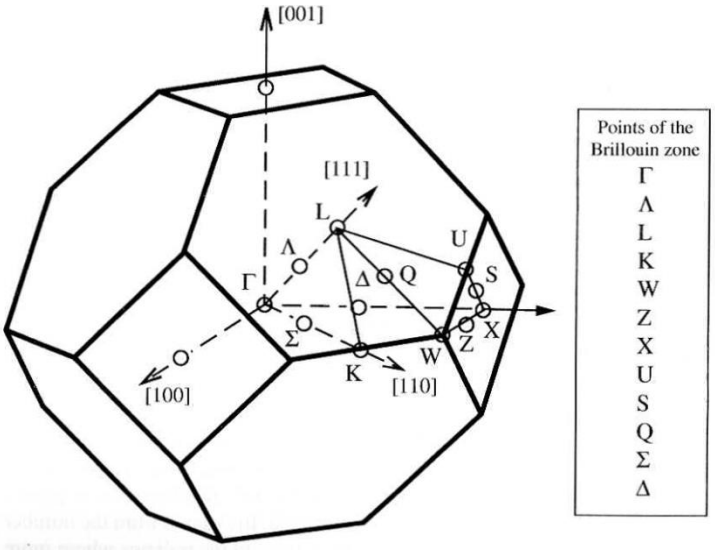

Figure 2.2: Lattice structure for a Face-Centred Cubic (FCC) lead chalcogenide showing Brillouin zone and its points [3].

Lead chalcogenides are typically opaque in appearance and have proven to be quite brittle in nature, tending to cleave at low temperatures. Interestingly however, this cleavage virtually vanishes at higher temperatures (above 700°C, 350°C and 300°C for PbS, PbSe and PbTe respectively [4]).

Researches have proven that the covalent bonding is more dominant bond in lead chalcogenides [3]. This was demonstrated through undertaking experiments on the phenomena of carrier scattering, which predicted that crystals with primarily ionic bonds should produce carrier scattering by optical phonons and not the acoustical. It was demonstrated that carrier scattering in lead chalcogenides was produced as a

result of acoustic and optical phonons. The reason the covalent bonds are more abundant in lead chalcogenides could possibly be due to their strong polarizability of all compounds with the cubic lattice structure. Tellurium, selenium and sulphur ions are widely considered to be able to undergo manipulation with minimal effort. Hence, the ionic bonds in chalcogenides alloys should be significantly weaker.

What distinguishes Pb chalcogenides from other semiconductors is their interestingly different electronic and transport properties, such as small band gaps, low resistivities, large carrier mobilities and positive temperature coefficients [5, 6]. Further research into these key properties through several optical and electrical measurements has led to the development of applications containing lead based chalcogenides for infrared lasers and detectors, thermophotovoltaics [7] and thermoelectrics [8-10] that results in a NASA Mars rover mission [11].

2.2. Band gap of lead chalcogenides

The band gap of a semiconducting material is known as the energy difference that separates the top of the valence band and the bottom of the conduction band. This difference in energy is the exact amount that must be provided to an electron in the valence band of the material, allowing it to move up to the conduction band. There are two available transitions that the electron can take when transporting to the conduction band. A direct band gap arises when the electrons and holes have equivalent momentum in the conduction and valence bands (Figure 2.3(a)). This match up in momentum allows a photon to become released from the electron. However when the momentum of the electrons and holes is not equivalent and the conduction band is shifted from the valence band, an indirect band gap occurs (Figure 2.3(b)). This difference in momentum involves the use of the phonon that should have been released from the electron to help balance the momentum in the crystal lattice [3].

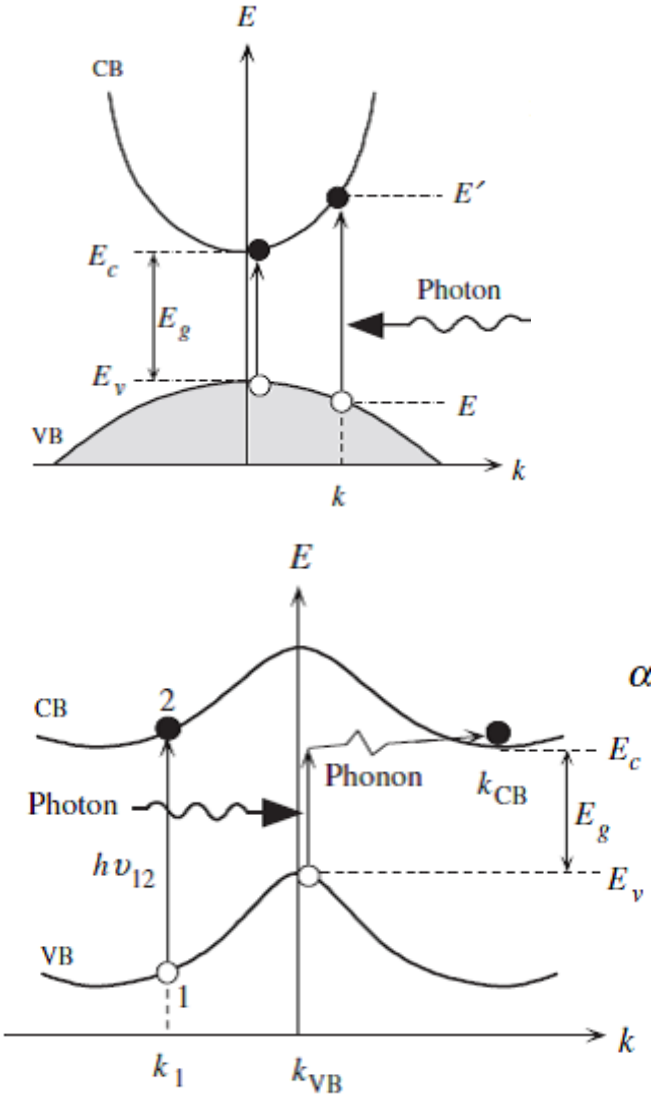

Figure 2.3: (a) The direct transition of an electron from the valence band to the conduction band (b) the phonon assisted indirect transition of an electron from the VB to CB. E_C is the conduction band energy, E_V is the valence band energy, k is the electrons wave vector, hv is the photon energy, E and E' are the initial and final energies of the electron [12].

The band gaps of modern semiconductors have recently become considered one of the integral properties for the design and uncovering of innovative applications in materials science. For instance, a significant enhancement in the thermoelectric performance of materials has been achieved through tuning the electronic band structure of lead chalcogenides [13, 14].

An intrinsic (or undoped) semiconductor is a pure semiconductor that has not been exposed to external impurity atoms. This results in the same number of electrons in the conduction band as there are holes in the valence band for this semiconductor. The doping level of the material is determined by its intrinsic defect level, rather than the impurities present. A pure semiconductor's intrinsic defect level can alter due to numerous factors such as sample preparation, stoichiometric ratios and energetics from defect formation. An extrinsic (doped) semiconductor requires the replacement of pure atoms from the intrinsic semiconductor, with impurity atoms of a different charge state. This is known as substitution and results in the formation of additional electrons or holes to the lattice, with the purpose of balancing charge neutrality [3].

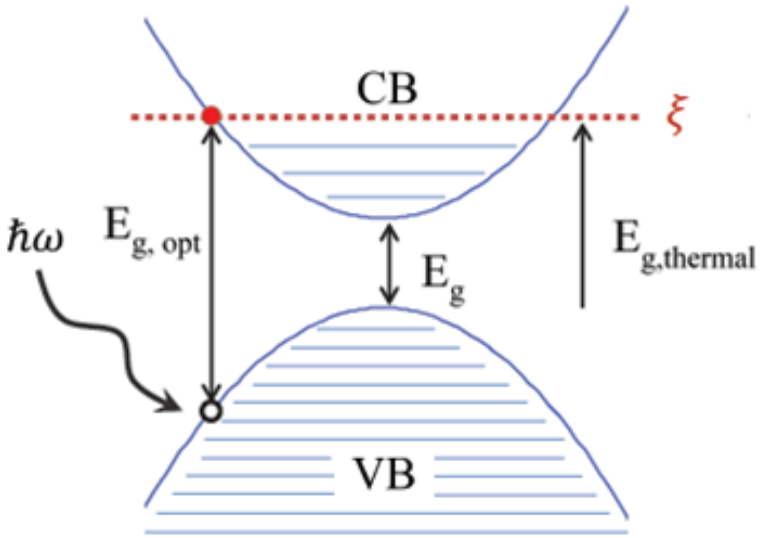

Figure 2.4: Visual representation of the alteration in optical band gap ($E_{g,\ opt}$) due to the Burstein-Moss shift [15].

A p-type semiconductor is formed when the introduced impurity atom has less valence electron's than the intrinsic semiconductor lattice, producing additional holes. However an n-type semiconductor is formed when the introduced impurity atom has more valence electrons than the intrinsic semiconductor lattice, introducing additional electrons in the conduction band. Extrinsic doping produces different electrical properties compared to intrinsic semiconductors; hence this technique is extensively used in thermoelectric materials for optimization of thermoelectric conversion

efficiency (zT). Although majority of practical applications require heavily doped materials (10^{19} – 10^{20} cm^{-3}), the ability to estimate their band gap, using optical measurements, becomes much more complicated due to the attributed free carrier contributions. Significant differences in the calculation of the material's band gap occur, roughly to the value of the Fermi level, ξ. This observed increase in optical band gap through the involvement of extrinsic samples is known as the Burstein-Moss shift and shown in Figure 2.4. Therefore, intrinsically doped samples should be prepared for optical band gap measurement, opposed to extrinsically doped samples [15].

2.3. Lead chalcogenide alloys

The pseudo-binary phase diagrams of ternary PbSe-PbTe, PbS-PbSe and PbS-PbTe systems are shown in Figures 2.5 to 2.7 respectively. The minimum in the liquidus and solidus curves is caused by the positive deviation from the ideal solution in the solid. Hence at high temperatures, complete solubility is observed. At lower temperatures however, this single soluble solution may be split up into two separate stable solutions. This is known as a miscibility gap and is present only in the ternary PbS-PbTe system (Figure 2.7), whereas, ternary systems of PbS-PbSe and PbSe-PbTe show solid solution over entire composition range below 1200 K.

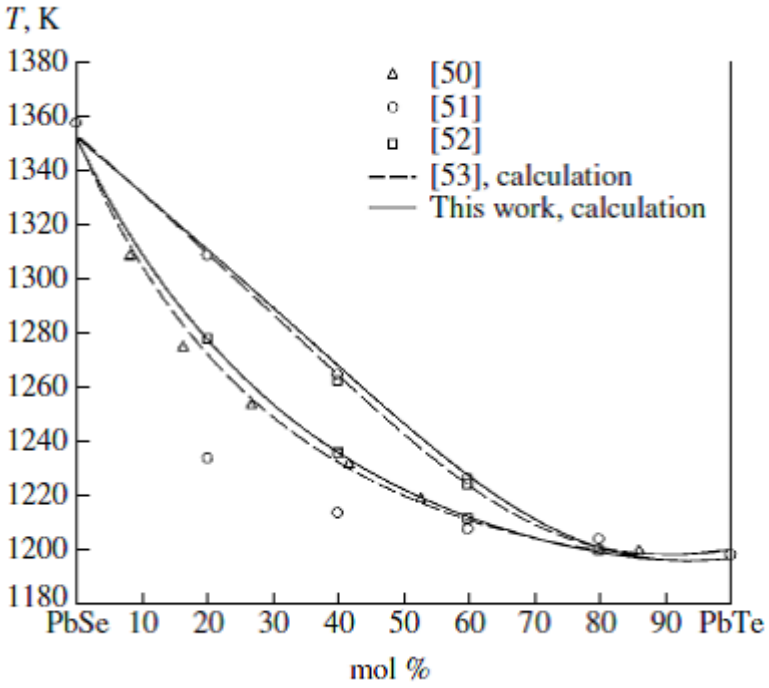

Figure 2.5: Phase diagram for $PbTe_xSe_{1-x}$ system [1].

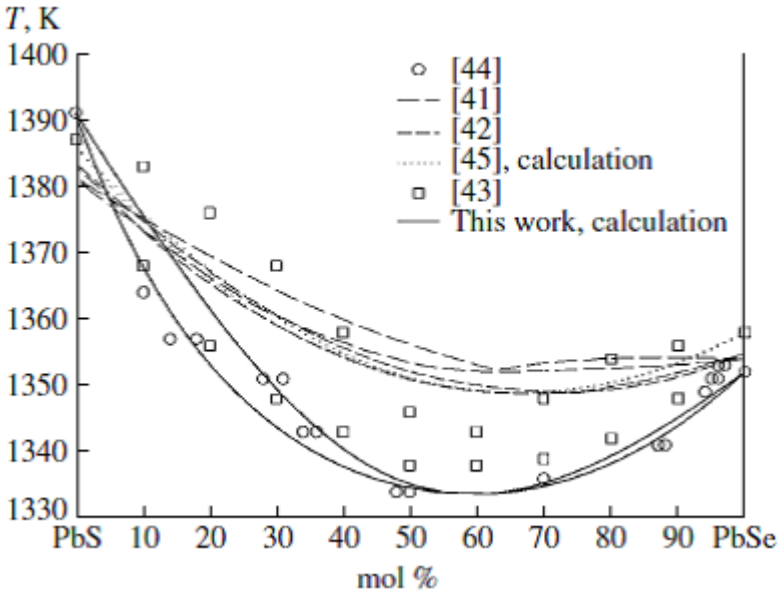

Figure 2.6: Phase diagram for $PbSe_xS_{1-x}$ system [1].

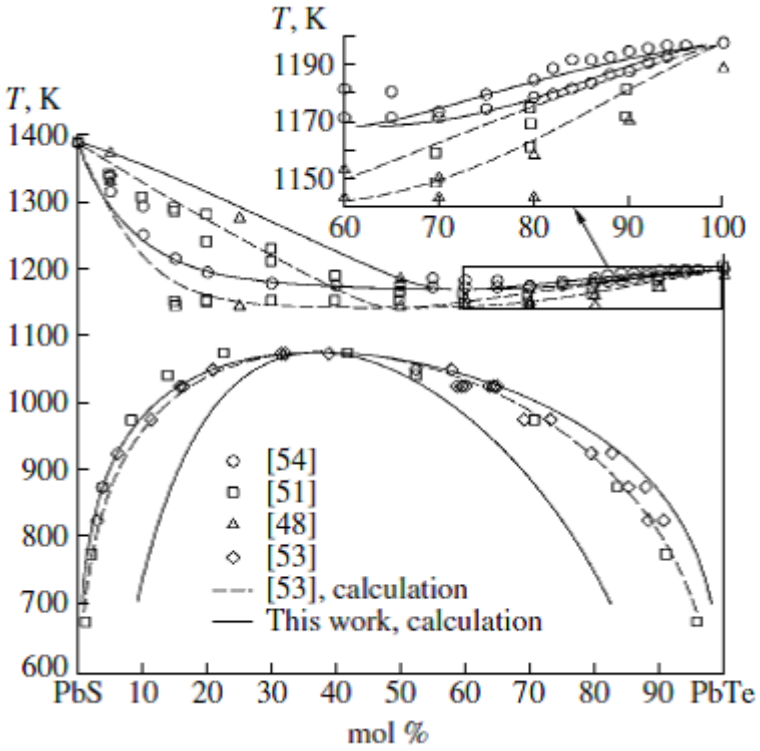

Figure 2.7: Phase diagram for $PbTe_xS_{1-x}$ system [1].

The liquidus curves for pseudo-ternary PbTe-PbSe-PbS system are provided in phase diagram shown Figure 2.8. It is evident that the miscibility gap maxima, where two phases begin to occur, steadily shifts to lower temperatures from 1050 to 700 K with increasing the PbSe content. The compositions of the samples fabricated for experimental analysis have been clearly labelled on the quaternary phase diagram. These compositions were specifically identified in order to avoid this miscibility gap and ensure no secondary phases were formed throughout the experimental process, as this is believed to give inaccurate measurements of the band gap [16].

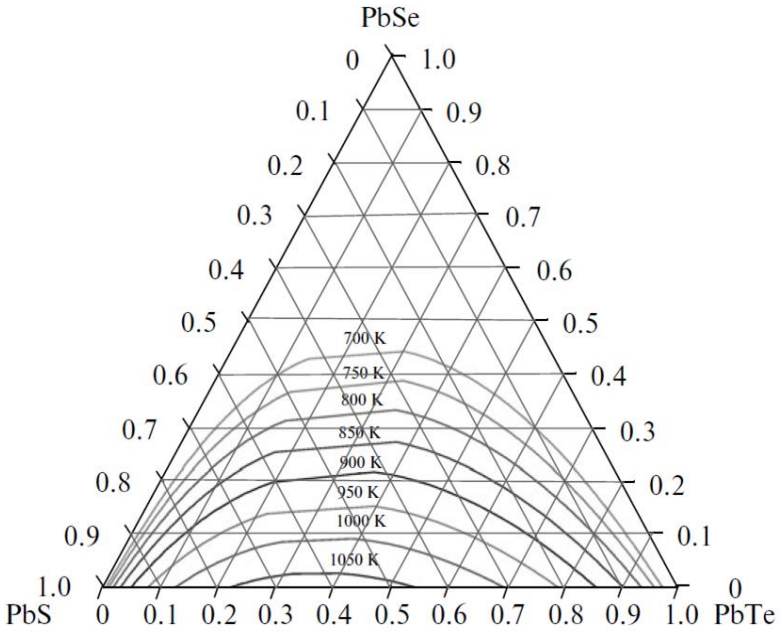

Figure 2.8: The quaternary phase diagram for PbTe-PbSe-PbS [17].

2.4. Electronic band structure of lead chalcogenides

The electronic band structure of lead chalcogenides have been discovered as a highly complex set up which differs greatly from traditional semiconductors [3, 13, 18, 19]. PbTe contains a conduction band and two valence bands in its unique structure. The light valence band (L) occurs at the L point located below the conduction band and the heavy band (Σ) is at an offset (ΔE) to the L band located on the Σ line. It has been shown in previous studies that a reduction in the valence band offset (ΔE), also known as band convergence, leads to increased thermoelectric properties of PbTe, PbSe and PbS. However the temperature at which this band convergence occurs is still under investigation and not mutually agreed.

2.4.1. Single Parabolic Band (SPB) model

The single parabolic band (SPB) [20] is a model curve produced to fit the data points on a graph where the absolute Seebeck coefficient ($|S|$) is plotted in relation to the Hall carrier concentration (n_H). The Seebeck part of the model is applied under Equation 2.1:

$$S = \frac{k_B}{e}\left(\frac{(2+\lambda)F_{\lambda+1}(\eta)}{(1+\lambda)F_{\lambda}(\eta)} - \eta\right) \qquad 2.1$$

Where S is the Seebeck coefficient, k_B is the Boltzmann constant, e is the electric charge, λ is the energy dependent relaxation time of carrier ($\lambda = 0$), η is the reduced chemical potential and F_λ is the Fermi integral. The Hall carrier concentration (n_H) section is produced using Equation 2.2:

$$n_H = 4\pi \left(\frac{2m^* k_b T}{h^2}\right)^{3/2} \frac{F_{1/2}\eta}{r_H} \qquad 2.2$$

Where the effective mass (m^*) is equal to $1.86m_e$ and r_H is the Hall factor [20]. It is possible to attain important properties of the material using the SPB model such as the lattice thermal conductivity (κ_L), effective mass (m*) and deformation potential (E_{def}) which measures the amount of electron scattering by acoustic phonons. Hence this SPB model is exceptionally helpful when estimating the required values for obtaining the optimal zT of a new material, since it can be simply produced from minimal experimental data.

2.4.2. Multiple Bands

Although the single parabolic band method can be used to describe electronic transport properties of a range of materials, the multiple electronic bands exists in the majority of semiconductors including lead chalcogenide alloys. For instance, the presence of these multiple electronic bands is assumed to be responsible for the significantly large thermoelectric efficiency (*z*T) in numerous lead chalcogenide systems such as PbTe [11, 13, 14], PbSe [21] and their alloys [6]. When this additional electronic band exists, the electrical conductivity of each band is added together while the Seebeck coefficient of each band remains at its original high value. This dramatic increase in electrical conductivity produces a superior zT, especially when the electronic bands are converged and contain occupied states. Band convergence occurs due to the multiple valence bands aligning at the same energy level and this phenomenon has been demonstrated to produce an increase in thermoelectric performance most successfully in the PbTe system [22], and more recently in the quaternary chalcogenide systems [23].

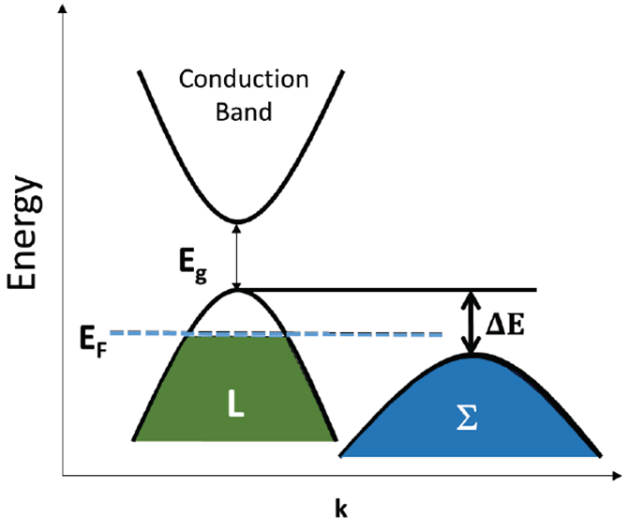

Figure 2.9: The multiple bands present for p-type lead chalcogenides include a light valence band (L) positioned directly under the conduction band, and a heavy valence band (Σ) which is offset from the conduction band [6].

PbTe, PbSe and PbS each have two valence bands which are thought to be separated by an energy difference of approximately 0.15, 0.25 and 0.5 eV respectively at 300K, although the exact difference in energy is an ongoing discussion [12, 13, 24]. The valence band closest to the conduction band at 300K is labelled the light band (L) and the other valence band as a separate heavy band (Σ) shown in Figure 2.9. This energy difference between the light and heavy bands (L – Σ) is known as the valence band offset (ΔE), which has been shown to reduce with increasing temperature and alloying of lead chalcogenide materials [25].

2.4.3. Temperature Dependence of band structure

The valence band offset for lead chalcogenides is believed to be altered as a function of temperature, producing converged bands at a certain temperature. The specific temperature at which this band convergence is achieved was previously thought to be approximately 400 K for PbTe as stated by Tauber et al. [22] A recent study however, suggests the temperature at which no valence band offset exists is closer to 700, 900 and 1000 K for PbTe, PbSe and PbS respectively [6, 26].

2.4.4. Effect of alloying on electronic band structure

The manipulation of electronic band energies has been achieved through alloying of the lead chalcogenide materials [8-10, 13, 14, 18, 21, 27, 28]. This alloying results in the enhancement of thermoelectric properties due to the possibility of band convergence, as discussed earlier, and can also be accredited to the minimization of lattice thermal conductivity from phonon scattering [2, 9, 13-15, 21, 28-31]. The Seebeck coefficient of a semiconductor can be drastically reduced due to minority carriers as they are provided with thermal energy to jump up from the valence band to the conduction band. This factor combined with the associated increase in the electronic thermal conductivity due to alloying [32-34], results in an peak at zT values as a function of temperature. If the band gap of semiconductors is widen, this maximum zT can be further increased [33]. It has been previously shown that alloying lead chalcogenides with materials of a larger band gap such as MgTe [35, 36] and CdTe [19, 37] produces a higher *z*T with rising temperature (Figure 2.10).

However, the tuning of electronic band structure by alloying is not limited to thermoelectric applications. Band engineering has shown to improve the performance of materials such as SiGeSn in transistors [38], $GaN_xAs_{1-x}/GaBi_xAs_{1-x}$ for lasers [39] and AlGaN in UV-LEDs [40].

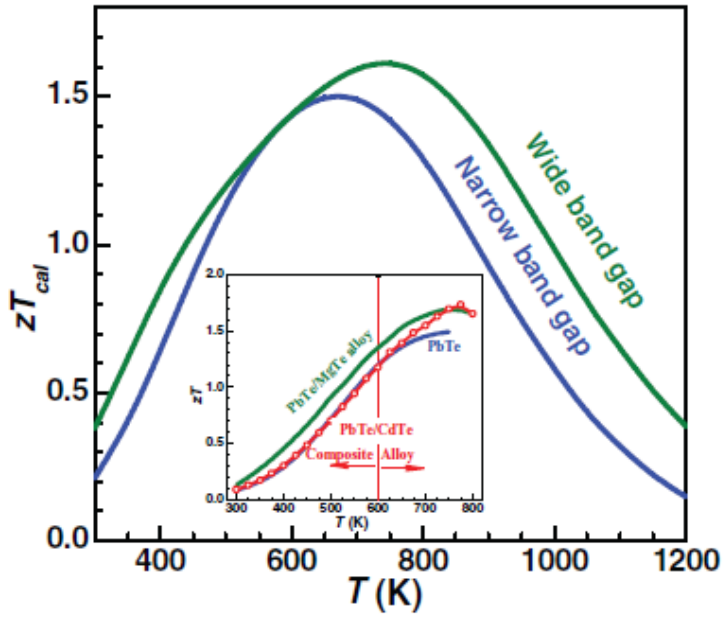

Figure 2.10: A calculated model showing how widening the band gap of a material due to alloying can increase the maximum zT [14].

2.5. Techniques for Measuring Band Gap

Optical measurements such as absorption edge, photoluminescence and photoconductivity have been proven as the most accurate and preferred method in measuring the band gap of a semiconductor [6, 21, 29, 41]. In order to measure the optical absorption edge, the powdered sample is exposed directly to light of different frequencies ($E = \hbar\omega$) which are able to be absorbed by the electrons available in the valence band. No absorption occurs if the photon energy provided by the light is smaller than the band gap of the material. If the photon energy is equal or greater than the band gap however, a sharp increase in the absorption coefficient (α) will be observed due to the electrons in the valence band being provided with enough $\hbar\omega$ to excite them toward the conduction band. Figure 2.11 shows the photon energy where this increase in the absorption coefficient starts usually provides a good estimation of the optical absorption edge [6, 15, 42].

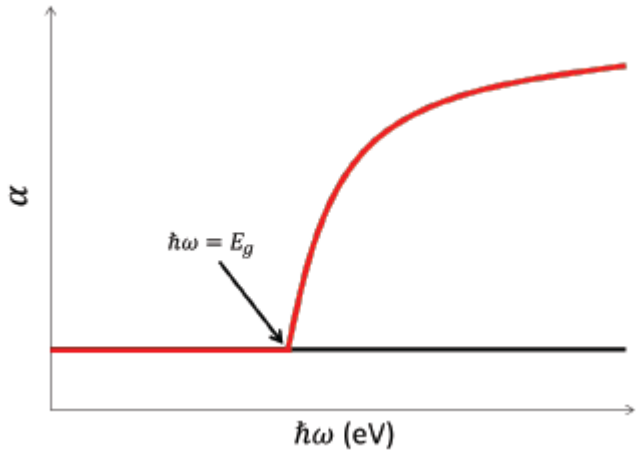

Figure 2.11: A sudden increase in absorption occurs when the energy of the photon ($\hbar\omega$) reaches the band gap energy (E_g) [25].

Rough approximations for the band gap energy of a semiconductor are extremely helpful no matter whether it is obtained from optical or electronic data. However through comparing and contrasting the different techniques for determination of the

band gap energy, optical measurements are the most precise and simplest method, particularly for materials with temperature dependent band gaps such as the lead chalcogenides. Optical absorption edge data has also been proven to provide sensitive measurements by showing small shifts in optical band gap energy with incremental changes in carrier concentration. This shift to higher energy is known as the Burstein-Moss shift that is explored in Section 2.2.

2.5.1. Photoluminescence Excitation Spectroscopy (PLE)

The electron-hole pair created when a semiconductor absorbs the photon undergoes the recombination and emits a photon as illustrated in Figure 2.12 during the photoluminescence (PL) process. The recombination process occurs very quickly and the released photon has the energy corresponding to the energy of inter band transition, the band gap energy.

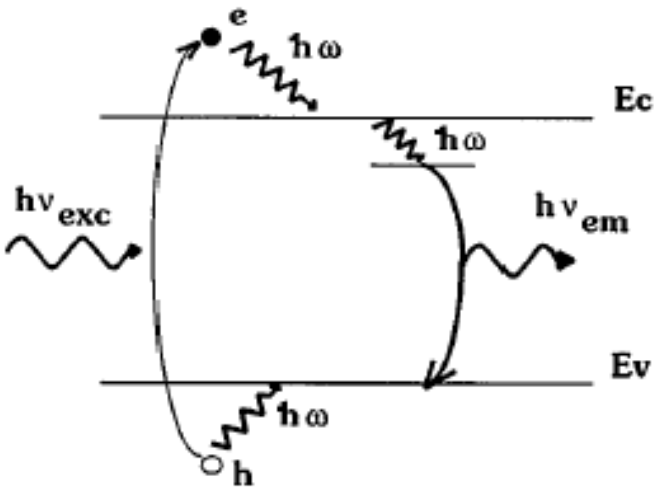

Figure 2.12: Diagram of the photoluminescence process where an electron is excited from the valence to the conduction band. The electron then releases a phonon by recombination of equal value to the semiconductors band gap energy [41].

For this technique the detector is held at the photoluminescence (PL) maximum energy, where the energy of the excited photon can be scanned using the excitation monochromator. The electron-hole pair is formed when the excited photons energy rises past the band gap energy (E_g). This electron-hole pair is then able to radiatively

recombine instantly using the small impurities present in the material and produce an energy equivalent to the band gap for the material [41].

This data is represented in the form of a photoluminescence excitation (PLE) spectrum where the photon energy is plotted against the optical absorption coefficient ($\alpha h\omega$). If the recombination's of the electron-hole pairs are negligible and *d* is the width of the layer, then the following equation can be assumed:

$$I_{PLE} \propto \Delta n \propto (1 - e^{-\alpha d}) \qquad 2.3$$

Where the intensity of the PLE (I_{PLE}) is proportional to the quantity of electron pairs, which is also proportional to the amount of excited photons absorbed at the sample surface. A more simplified equation can be produced dependent on the thickness of the layer (*d*). If *d* is thin, the absorption will follow the shape of the PLE spectrum and Equation 2.3 can be expanded to:

$$I_{PLE} \propto \alpha d \propto \alpha \qquad 2.4$$

Here the PLE spectrum can still be used to determine the absorption but not quantitatively. If the layer is sufficiently thick, the absorption tends to move monotonically and the exponential will move to zero in the form of an asymptote:

$$I_{PLE} = I_{\infty}(1 - e^{-\alpha d}) \qquad 2.5$$

Where the asymptotic intensity of the PLE spectrum I_{PLE} at high temperatures is given by I_{∞}. The absorption coefficient is measured quantitatively from the application of Tauc's method (Equation 2.7) to this spectrum.

Although this technique has shown to give accurate estimations of the band gap for semiconductors [41], the range of measurement for this technique is a limiting factor as it detects energies between 1.40 and 1.80 eV and lead chalcogenides have band gaps between 0.27 and 0.42 eV. The sample preparation is also an issue for this technique since the samples were epitaxial layers grown on substrates. This would increase experimental time dramatically with no real benefit compared to other techniques.

2.5.2. Ultraviolet-Visible (UV-Vis) Spectroscopy Technique

The UV-Vis spectroscopy technique is used to estimate the band gap energy in semiconductors. The range of measurement for UV-Vis spectroscopy lies between 50,000 – 12,500 cm^{-1} wavenumbers. This range is converted to electron volts (eV), as this is the unit the band gap energy will finally be measured, using the Planck relation [43]:

$$E = hv = \frac{hc}{\lambda} = hc\tilde{\nu} \qquad 2.6$$

Where E is the energy in electron volts (eV), h is the Planck constant (eV.s), v is the frequency (s^{-1}), c is the speed of light ($m.s^{-1}$), λ is the wavelength (cm) and $\tilde{\nu}$ is the wavenumber (cm^{-1}). This conversion produces a range of 1.55 eV – 6.20 eV. This lies outside the predicted bang gap energy of all three lead chalcogenide alloys (Table 2.1). Although UV-Vis spectroscopy is very similar to FTIR spectroscopy in terms of the principles and experimental technique, the range of measurement for this procedure (1.55 eV – 6.20 eV) does not match the region for the band gap energy of lead chalcogenide alloys (0.25 – 0.45 eV).

Table 2.1: Summarises the band gap of binary PbTe, PbSe and PbS [3, 4].

Compound	Band Gap (eV)
PbTe	0.32
PbSe	0.29
PbS	0.41

2.5.3. Fourier Transform Infrared (FTIR) Spectroscopy Technique

FTIR spectroscopy is able to obtain absorption data in the range required for the lead chalcogenides and their alloys. The raw data is obtained at wavenumbers between 6000 – 400 cm^{-1} in the mid infrared range (MIR). Adopting Equation 2.6 for Planck's conversion [43] from wavenumber (cm^{-1}) to electron volts (eV), produces a range of 0.05 – 0.73 eV which is ideal for PbTe, PbSe, PbS and their alloys. FTIR spectroscopy can be performed on a range of samples such as solids, liquids, gels or coatings. This

technique requires minimal sample preparation and produces quick, repeatable measurements for immediate data analysis.

The method undertaken in order to determine this band gap energy was via optical measurements, where the diffuse reflectance of the powder was determined. This was achieved by obtaining all the light that was reflected off the powder, excluding the specular reflected light (diffuse reflection).

The band gap of each sample could then be determined using the Tauc method [42],

$$(\alpha\hbar\omega)^n = B\,(\hbar\omega - E_g) \qquad 2.7$$

where α is the absorption coefficient, $\hbar\omega$ is the energy of the incoming photon, and n is equal to either ½ or 2 depending on whether the transitions are indirect or direct. The n is assigned the value of 2 (direct gap) for Tauc fits here, because when n = ½ (indirect gap) is fitted the resulting optical gap is approximately 0.03 to 0.05 eV below the direct optical gap found when n = 2 for each sample. This energy is around the energy of phonons in this material, hence why the n = ½ fit can be attributed to phonon-assisted transitions from L valence to L conduction bands – as proposed by Scanlon [4].

B is a frequency dependent constant

$$B = q^2 x^2_{vc} (2m_r)^{3/2} / \lambda_0 \varepsilon_0 \hbar^3 n \qquad 2.8$$

q is the elementary charge, x_{vc} is a matrix element (units of length and in same order of magnitude as lattice constant), m_r is the reduced mass, ε_0 is the vacuum permittivity, $\hbar$ is the reduced Planck's constant and n is the index of refraction.

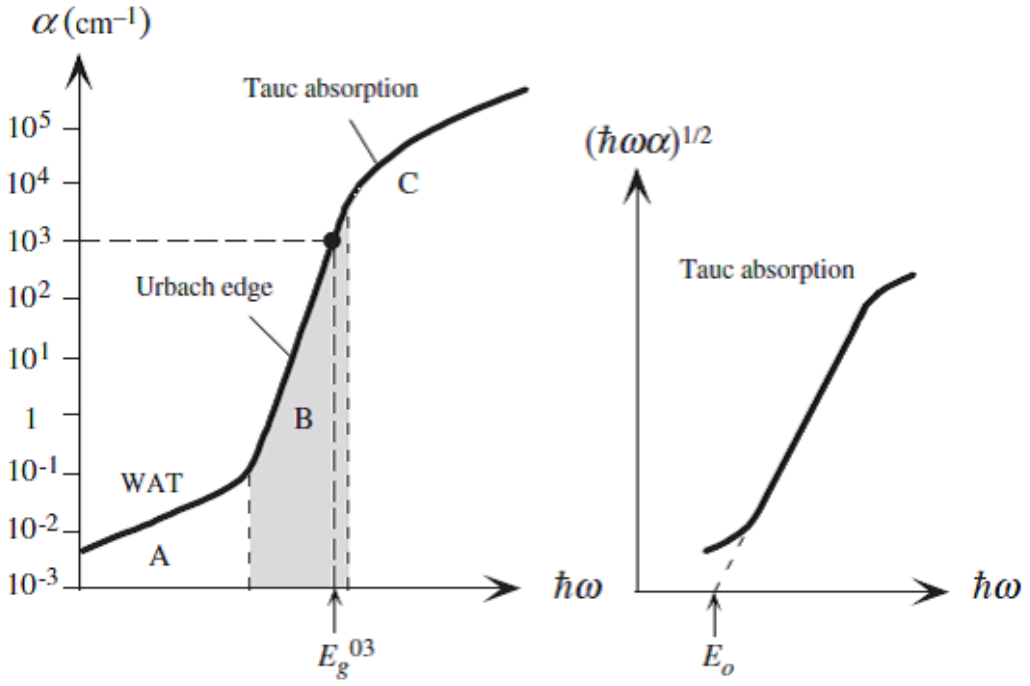

Figure 2.13: Three areas of optical transitions in amorphous semiconductors near the absorption edge [12].

The three types of optical transitions present in lead chalcogenides at the absorption edge are labelled by areas A, B and C as shown in Figure 2.13. Each individual area can be described by its transitions between tail states, tail to extended states, and extended states. Areas A and B occur at energies less than the band gap (E_g) and area C appears when the energy rises above the band gap.

Area A is also known as the weak absorption tail (WAT) due to its occurrence when the absorption coefficient is less than 0.1 cm^{-1}. In this range the optical absorption is determined by shifts between tail and tail states which occur due to defects. The density of these defects can be approximated for the sample by the maximum absorption in this area. When the absorption coefficient is between roughly 0.1 and 10,000 cm^{-1} the transitions to and from the extended states start to occur. This is labelled area B in Figure 2.13 and involves transition from either just above the valence band boundary up to the conduction band or from the valence band to just below the conduction band boundary. This region is known as the Urbach edge because the absorption coefficient (α) varies according to the Urbach rule [44]:

$$\alpha = \alpha_0 \exp[(h\nu - E_0) / \Delta E] \quad 2.9$$

Where the constants α_0, E_0 and ΔE (Urbach width) are all material dependent components. The Urbach width has shown to be linked to the width of the tail states and could be compared to the Urbach width of other semiconductors. This rule was first investigated for alkali halides [44, 45], however it has now been reported for degenerately doped crystalline semiconductors and basically every amorphous semiconductor. As mentioned above, area C appears at energies exceeding the band gap and is dependent on the extended to extended states optical transitions. In this section of the curve the absorption coefficient tends to cohere with Tauc's method[42] (Equation 2.7) for the optical band gap demonstrated by the right side of Figure 2.13.

The proportionality of the absorption coefficient (α) can be determined using the Kubelka-Munk function [46], where:

$$\alpha / S = F(R_\infty) = (1- R_\infty)^2 / 2R_\infty \quad 2.10$$

$(\alpha\hbar\omega)^n$ was plotted against $\hbar\omega$ and extrapolated to zero.

2.5.3.1. Diffuse reflection of powdered samples

Single interface reflection uses plane waves to explain the light. Diffuse reflection measurements differ from this single interface approach by describing the light as a flux. Light flux can be defined as the upward or downward intensity that is travelling through a material with thickness dz [46]. The Kubelka Munk theory involves the existence of two fluxes, an upward directional flux and a downward directional flux. Using this knowledge, the diffuse reflection of the powder can be defined as the upward directional flux when the distance between the particles is greater than the material thickness.

2.5.3.2. Absorption

When the diffuse reflectance of the powdered sample has been acquired, the absorption of the material can be determined using the Kubelka Munk Method. It is

worth noting that we are focusing on the absorption of the material and not the absorptance. Absorptance involves scattering and other phenomena that don't require the light to be absorbed by the sample i.e. all light that is not specularly reflected (R) or transmitted (T) [47]:

$$A = 1 - T - R \tag{2.11}$$

The general equation for the absorption of a material (α) is given in relation to wavelength (λ) and the imaginary coefficient of the index of refraction (κ):

$$\alpha = \frac{2\omega\kappa}{c} = \frac{4\pi\kappa}{\lambda} \tag{2.12}$$

Chapter 3

Experimental Techniques

3.1. Materials Fabrication

The polycrystalline samples of lead chalcogenides are synthesized by melting of high purity starting materials and homogenizing the melt above the melting point of final compound. The starting materials of polycrystalline PbSe and PbS were synthesized through mixing stoichiometric ratio of high purity Pb (99.999%), Se (99.999%) and dried S (99.9%) in vacuum sealed quartz ampoules and reacting them at high temperatures. The polycrystalline samples of ternary and quaternary compounds of $PbTe_{1-x}Se_x$, $PbSe_{0.1}Te_{0.9-x}S_x$ (x = 0, 0.05, 0.08 and 1) and $PbSe_{0.35}Te_{0.65-x}S_x$ (x = 0, 0.05, 0.10, 0.15, 0.20, 1) were prepared through mixing stoichiometric ratio of the high purity PbSe, PbS, Pb and Te in a vacuum sealed quartz ampoule, with a total mass of 10 g and heating them to 1373 K over 12 hours, followed by 6 hours homogenizing and cooling to room temperature in the furnace. The resulting ingots were hand ground to powder for characterization.

Spark plasma sintering (SPS) is a technique undertaken to produce a solid disc shaped sample as a result of an applied uniaxial pressure and pulsating electric current [48]. SPS enables the samples to be exposed to increased heating gradients and minimizes the likelihood of intrinsic defects being produced throughout the process. The powdered sample fabricated previously can be placed in the sintering die between the two punches as shown in Figure 3.1. The upper and lower electrode punches are then compressed to approximately 5 MPa to hold the sample in position, where the chamber can then be closed and evacuated. This powder is sintered at 773K for 1 hour at an axial pressure of 40 MPa under vacuum. The sintered samples were used to determine the thermal conductivity and room temperature electrical resistivity and Seebeck of samples.

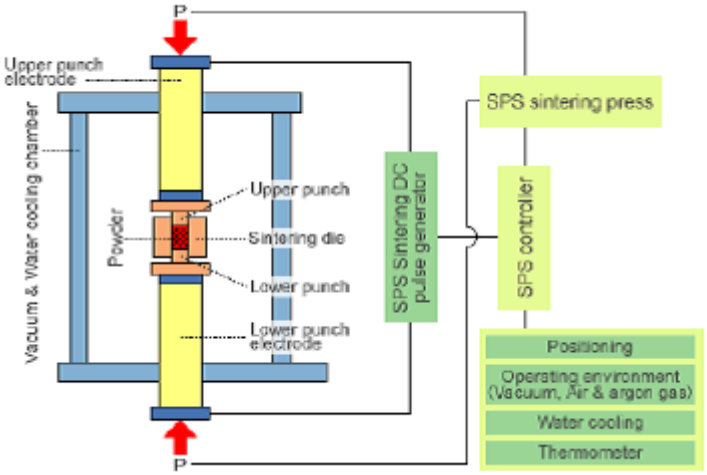

Figure 3.1: Visual representation of the spark plasma sintering (SPS) technique [48]

3.2. Materials Characterisation

3.2.1. X-ray Diffraction

XRD analysis was performed on the final samples to determine the crystallographic structure and composition using a GBC Scientific X-Ray diffractometer with Cu K_α radiation (λ = 1.544 Å, 40 kV, 30 mA). This technique involves the crystalline atoms of the sample causing the X-ray beam to be diffracted at various angles and is used to determine the specific structure and lattice parameters of the crystalline materials. The samples must first be prepared by grinding the ingots into an extremely fine powder using an agate mortar and pestle (identical to sintering preparation). A thin uniform layer of this powder is formed on a quartz substrate. The sample can then be mounted in the X-Ray diffractometer and scanned over 20° < 2θ < 110° at a rate of 1°/min. The X-rays expelled from the diffractometer are done so from a cathode ray tube which has been altered, so that concentrated monochromatic radiation is focused on the sample surface. The X-ray diffraction patterns are produced via constructive interference of these monochromatic X-rays with atoms in the lattice structure of a material, given by:

$$n\lambda = 2d \sin\theta \qquad 3.1$$

Equation 3.1 is known as Bragg's Law and describes the wavelength's relationship to

the angle of incidence and the d spacing of the atoms. Here n is the integer corresponding to the order of the diffraction peak, λ is the wavelength of the radiation, d is the distance between atoms in the crystal structure and θ is the angle of incidence. By producing a monochromatic X-ray of known wavelength to the powdered sample, all different angles of diffraction are recorded which correlate to the atomic distance between atoms of the sample. The composition of the sample can then be determined via the Rietveld method by comparing the recorded *d*-spacing's with a standard reference XRD pattern.

3.2.2. Band gap measurement

Diffuse Reflectance Infrared Fourier Transform Spectroscopy (DRIFTS)

Absorption edge measurements were recorded using a Shimadzu IRPrestige-21 Fourier Transform Infrared (FTIR) Spectrophotometer equipped with a Diffuse Reflectance attachment at 298 K. The spectra were monitored in the MIR region (6000 – 400 cm^{-1}) which when converted to electron volts (eV) using Planck's law [43] and Equation 2.6 gives a range of 0.05 – 0.73 eV which is perfect for the lead chalcogenides. Experiment was undertaken in a nitrogen atmosphere following pumping and releasing of the sample chamber multiple times. Each scan was referenced against both KBr standard samples and mirror standard at 298 K. The mirror was chosen as the reference for final calculations and experimental graphs as the data were basically identical without the impurity of the KBr. The measurement set up is shown schematically in Figure 3.2.

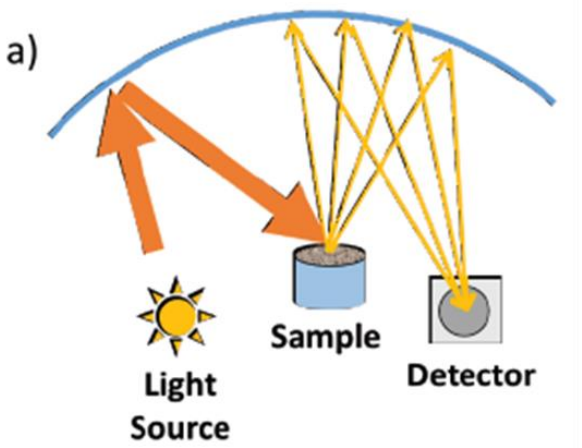

Figure 3.2: An illustration of measuring the spectral absorption using Diffuse Reflectance Infrared Spectroscopy Technique (DRIFT) [25]

The diffuse reflection of the powdered sample is measured. The light that alters by 180 degrees from the incident ray to the reflection ray is known as specular reflectance. When attempting to determine the diffuse reflectance of the sample, this specular reflectance is not included in the collected light from the powder. The degree of reflectivity is calculated by the ratio of the reflected light intensity to the incident light intensity:

$$R_{Sample}(\lambda) = \frac{I_{Sample}(\lambda)}{I_{Reference}(\lambda)} \qquad 3.2$$

Where $R_{Sample}(\lambda)$ is the degree of reflectivity of a sample, $I_{Sample}(\lambda)$ is the light intensity reflected from the sample and $I_{Reference}(\lambda)$ is the light intensity reflected from the reference material. In order to determine the absolute reflectance, the reference material must have 100% reflection coefficients [49].

This equation however, does not take into account the background light that is detected and hence makes the task of obtaining a reference material with 100% reflectivity almost impossible. In order to achieve a more accurate value for $R_{Sample}(\lambda)$, an extra measurement is taken where the incident light is removed allowing the background intensity to be quantified. This background intensity can then be subtracted from both the sample and reference intensities ($I_{Sample}(\lambda)$ and $I_{Reference}(\lambda)$ respectively). Finally, the new reflectance ratio determined should be multiplied by a reference reflectance that allows the exact absolute reflection ($R_{Sample}(\lambda)$) to be achieved.

3.2.3. Thermal Conductivity

Thermal conductivity is defined as a property that determines a specific samples ability to conduct heat. The thermal conductivity of the lead chalcogenides were measured using Equation 3.3 [50]:

$$\kappa = \rho D_T C_p \qquad 3.3$$

Where κ is the thermal conductivity, ρ is the density of the material (g.cm^3), D_T is the thermal diffusivity (cm^2.s^{-1}) and C_p is the specific heat capacity (J.K^{-1}). The process of calculating the thermal conductivity begins with measuring the thermal diffusivity (D_T) of each sample through the laser flash method. The Linseis LFA 1000 apparatus was used to measure the thermal diffusivity of sintered sample. The technique involves a ~2mm thick disc shaped sample being placed inside an electric furnace, where a laser pulse starts heating the surface of the material under vacuum. Figure 3.3 shows how the sample absorbs energy from the laser pulse at its top surface and the recorded temperature is taken from the bottom surface, known as a thermogram. The measurements are recorded using an infrared sensor as the temperature at the bottom surface increases from room temperature (298 K) to approximately 800 K, then back to room temperature.

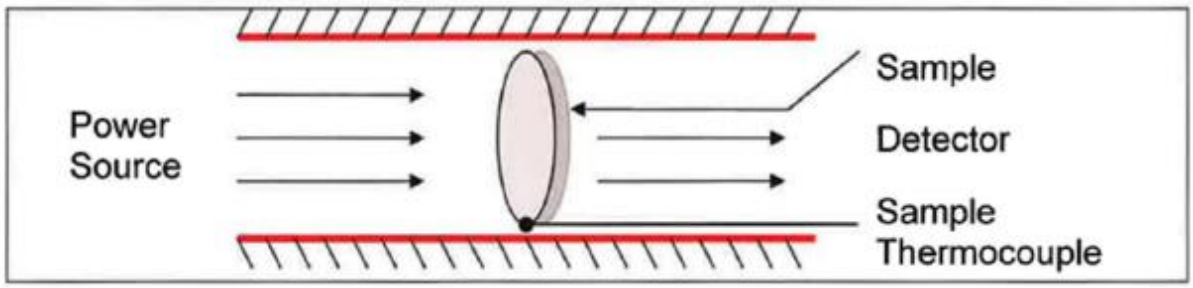

Figure 3.3: Visualisation of how the thermal diffusivity measurements are gathered using the laser flash method [2]

The density (ρ) is calculated using the measured weight and dimensions and specific heat capacity (C_p) is estimate from equation 3.5 in order to determine the thermal diffusivity of each sample. The density is calculated using the empirical formula:

$$\rho = \frac{m}{V} \qquad 3.4$$

Where the mass (m) and volume (V) are determined using the measured weight, thickness and diameter of the sample prior to thermal diffusivity measurement. The specific heat capacity was also estimated using an empirical formula [51] :

$$C_p(k_b\ per\ atom) = 3.07 + 4.7 \times 10^{-4} \times (T/K - 300) \quad 3.5$$

The introduction of the relative temperature increase to this procedure as appose to the use of properties like heat quantity and absolute temperature increase, provides dramatic increases in the speed and accuracy of the measurements using the laser flash method.

3.2.3.2. Temperature Dependent Seebeck and Resistivity

The band gap, E_g, of a thermoelectric semiconductor can be estimated in relation to the maximum Seebeck coefficient, $|S|_{max}$, through application of the Goldsmid-Sharp band gap equation [52]:

$$E_g = 2e|S|_{max}T_{max} \quad 3.6$$

It is evident when looking at Equation 3.6 that a maximum in the Seebeck coefficient would correspond to a maximum zT value. Hence determining the correct band gap and when bipolar effects begin to occur is integral in the optimization of zT for each specific material and its dependence on temperature.

The band gap, E_g, of a thermoelectric semiconductor can be estimated using measured electrical resistivity of the material as a function of temperature [25]:

$$\rho(T) = \rho_0 exp\left(-\frac{E_g}{2k_BT}\right) \quad 3.7$$

Where ρ is the electrical resistivity, T is the temperature, ρ_0 is a constant value related to the density of states and mobility of the material, E_g is the band gap of the sample and k_B is Boltzmann constant. Equation 3.7 allows the band gap to be determined from the room temperature electrical resistivity by graphing the natural log of resistivity against the inverted temperature. However the linear part of this graph may not occur if the sample is heavily doped, so this method requires measurements to be undertaken with intrinsic semiconductors (low carrier concentration).

Chapter 4

Band gap measurement of lead chalcogenide alloys

Lead chalcogenides have been used in electro-optical devices due to their narrow band gaps, large carrier mobilities and low resistivities. The physical properties of lead chalcogenides have been shown to vary significantly by alloying [9, 11, 29, 53]. Among physical properties, the band gap study of lead chalcogenide solid solution alloys has received little attention. The change in band gap of lead chalcogenide alloys with composition has commonly been considered a linear relationship [54, 55]. Through the application of advanced measurement techniques, it is now possible to determine whether bowing occurs in this system and what are the factors affecting it.

In this chapter, three chalcogenide systems of interest are analyzed for the band gap measurements: $(PbTe)_{1-x}(PbSe)_x$, $(PbTe)_{0.9-y}(PbSe)_{0.1}(PbS)_y$ and $(PbTe)_{0.65-y}(PbSe)_{0.35}(PbS)_y$. The ternary system of $(PbTe)_{1-x}(PbSe)_x$ determines the effect of PbSe content on the band gap of PbTe. It is previously [23, 54] shown that single phase PbTe-rich quaternary alloys of $(PbTe)_{1-x-y}(PbSe)_x(PbS)_y$ provide higher thermoelectric performance than ternary and quaternary lead chalcogenides due to obtained higher power factor and lower lattice thermal conductivity. The enhanced power factor is believed to be associated with larger band gap and energy band offset originated from PbS alloying. Here, the room temperature band gap of quaternary $(PbTe)_{0.9-y}(PbSe)_{0.1}(PbS)_y$ and $(PbTe)_{0.65-y}(PbSe)_{0.35}(PbS)_y$ systems are studied to elucidate the effect of PbS concentration on the band gap of ternary $(PbTe)_{1-x}(PbSe)_x$ alloys. The quaternary system, which contains higher concentration of PbSe, dissolves higher concentration of PbS [17, 56]. As will be discussed, the samples must be single phase for band gap measurements in order to produce accurate readings.

The chemical composition and structure of fabricated ingots are characterized with XRD. The lattice parameters were determined using Rietveld refinement prior to

determining the band gap using Diffuse Reflectance Infrared Fourier Transform (DRIFT) Spectroscopy. The measured room temperature band gaps are plotted as a function of composition variations. The results consistently differ from linear projection and show a deviation with a parabolic shape. The bowing parameter of curves are determined and factors influenced the degree of bowing is described in details.

4.1. Ternary $(PbTe)_{(1-x)}(PbSe)_x$ system

The X-ray diffraction patterns for samples of $(PbTe)_{(1-x)}(PbSe)_x$ (x= 0, 0.10, 0.15, 0.35, 0.50, 0.70, 0.85, 1.0), presented in Figure 4.1, show single phase compounds, indicating solid solution over whole composition range in PbTe-PbSe ternary system. No additional peaks are observed that could be assigned to a secondary phase. Figure 4.1 reveals an accumulative shift to the right angles in the 2theta with increased selenium content. This is originated from the replacement of the larger tellurium atom (140 pm) with the smaller selenium atom (120 pm) and becomes more prevalent at higher angles.

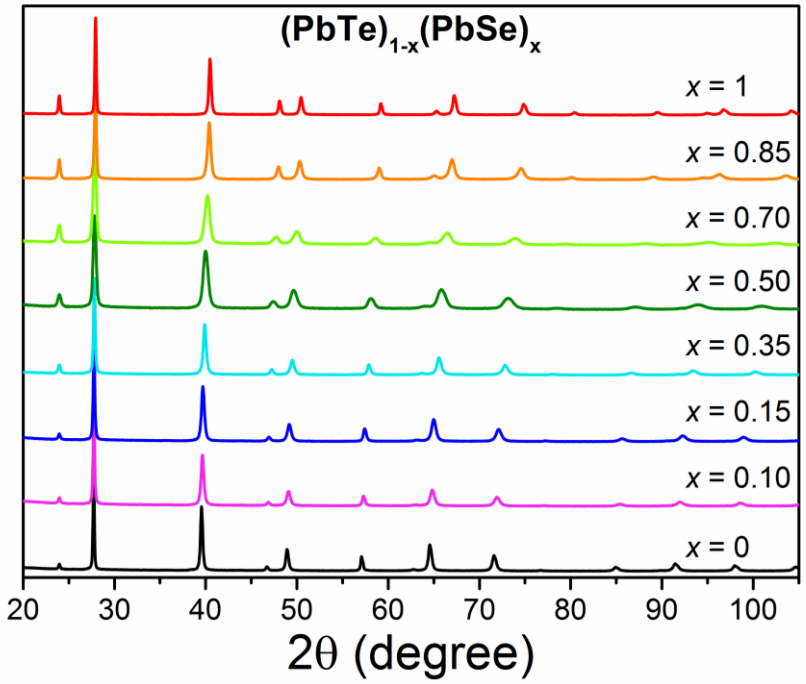

Figure 4.1: Powder X-ray diffraction patterns for ternary $(PbTe)_{(1-x)}(PbSe)_x$ (x= 0, 0.10, 0.15, 0.35, 0.50, 0.70, 0.85, 1.0) system.

The lattice parameters of single phase alloys are calculated using Rietveld analysis of the X-ray diffraction patterns in Figure 4.1. The pseudo-binary phase diagram of PbTe-PbSe (Figure 4.6) shows that PbTe and PbS form solid solution alloys over the whole composition range. Figure 4.2 confirms that the lattice parameters of $(PbTe)_{(1-x)}(PbSe)_x$ system changes linearly with composition and the variation of lattice parameter with composition follows Vergard's Law.

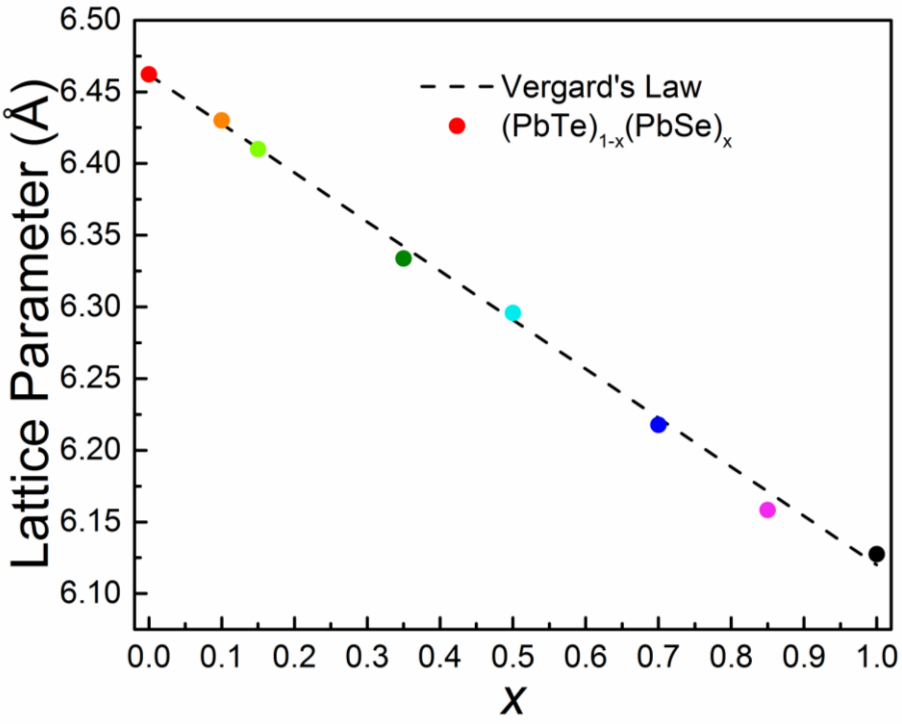

Figure 4.2: Lattice Parameters for ternary $(PbTe)_{(1-x)}(PbSe)_x$ (x= 0, 0.10, 0.15, 0.35, 0.50, 0.70, 0.85, 1.0) system as a function of PbSe content.

Since it has been confirmed through X-ray diffraction measurements and lattice parameter determination that the $(PbTe)_{(1-x)}(PbSe)_x$ samples are entirely single phase, the room temperature absorption edge spectra is measured using Diffuse Reflectance Infrared Fourier Transform (DRIFT) spectroscopy. Kubelka Munk transformations are performed on the raw data and the normalized spectra are shown in Figure 4.3. The absorption edge does not shift to higher energies in the linear fashion expected with increasing Te content.

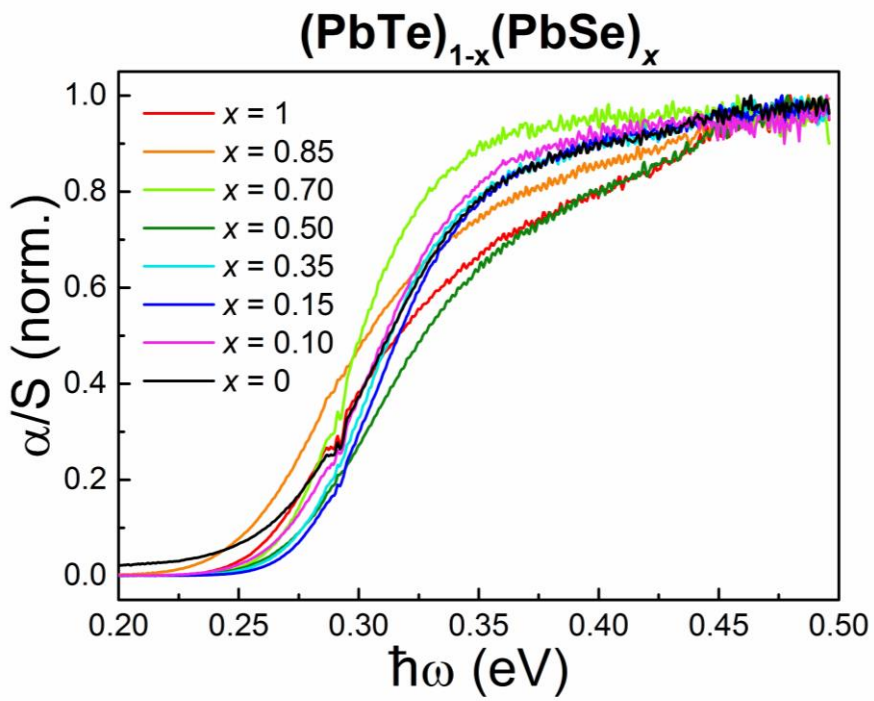

Figure 4.3: Normalized Kubelka Munk transformations for ternary $(PbTe)_{(1-x)}(PbSe)_x$ (x= 0, 0.10, 0.15, 0.35, 0.50, 0.70, 0.85, 1.0) system from raw data obtained using DRIFT spectroscopy.

The band gap of each sample can be determined through applying the Tauc transformations for direct gap semiconductors as shown in Figure 4.4. By extrapolating the linear section of the curve to zero, the band gap energy of each sample is determined.

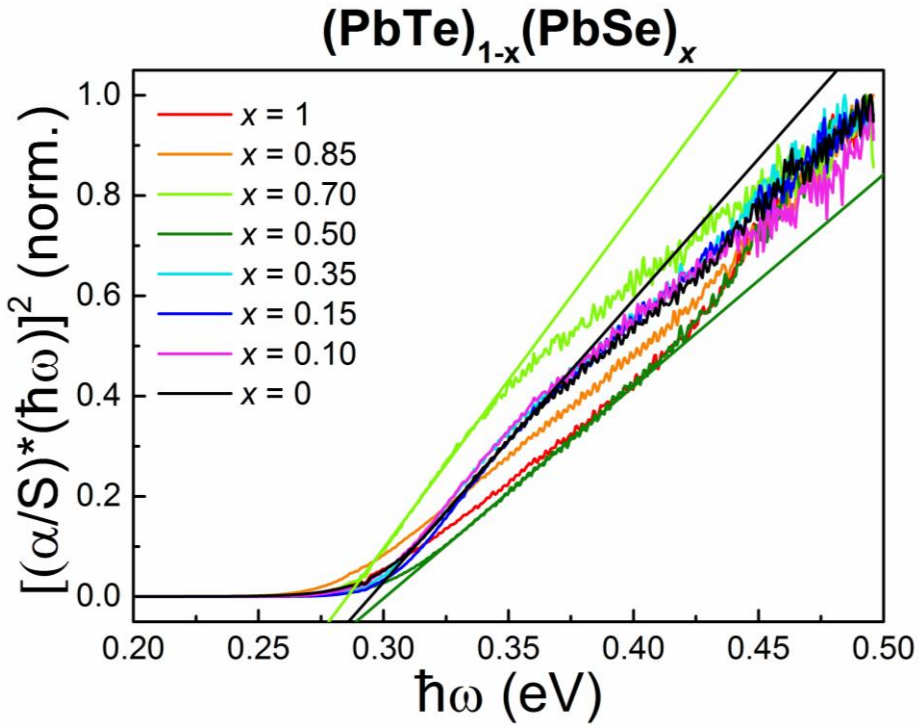

Figure 4.4: Normalized Kubelka Munk transformations ternary $(PbTe)_{(1-x)}(PbSe)_x$ (x= 0, 0.10, 0.15, 0.35, 0.50, 0.70, 0.85, 1.0) system from the application of Tauc method for direct gaps.

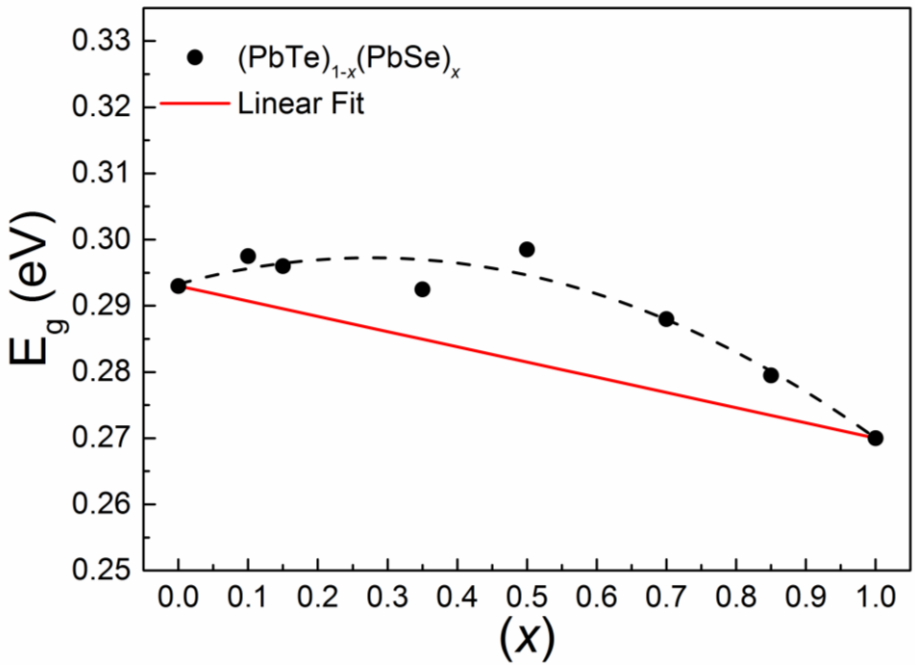

Figure 4.5: The direct band gaps for ternary $(PbTe)_{(1-x)}(PbSe)_x$ (x= 0, 0.10, 0.15, 0.35, 0.50, 0.70, 0.85, 1.0) system as a function of PbSe content.

Figure 4.5 depicts the non-linear change in band gap with composition in a slightly

more quantitative manner than Figure 4.3. Here it is evident that the band gaps of the alloys in the $(PbTe)_{(1-x)}(PbSe)_x$ system vary in a parabolic contour rather than the linear one expected. This deviation from the linear graph is due to a phenomenon known as the bowing effect.

4.1.1 Ternary Band Gap Bowing

The change in band gap of lead chalcogenide alloys with composition is generally supposed to be a linear relationship [55]. However our results challenge this widely accepted view and suggest that a positive bowing occurs by alloying. The nonlinear nature of the optical band gap with composition variation is not uncommon and has been observed in a number of classical semiconductor systems such as Si-Ge [57], InGaN, AlGaN and AlInN [58] and CdSe-CdTe[59].

The bowing parameter is described by the parabolic polynomial [60]:

$$E_{g,PbTeSe} = xE_{g,PbSe} + (1-x)E_{g,PbTe} - bx(1-x) \qquad 4.1$$

$E_{g,PbSe}$ and $E_{g,PbTe}$ are the non-degenerate band gap energy of the initial binary semiconductors and $E_{g,PbTeSe}$ is the band gap energy of the alloy material. The degree to which the curve deviates from the linear fit is described by the bowing parameter, b [61]. This parameter can be calculated by fitting a parabolic function through the experimental data gathered, as shown in Figure 4.5. This gives a bowing parameter of -0.052 ± 0.011 eV for $(PbTe)_{(1-x)}(PbSe)_x$ system. The bowing parameter is negative due to the inverted nature of the parabola for the ternary $(PbTe)_{(1-x)}(PbSe)_x$ system. It is approximately four times larger than the deviation of the band gap from the linear behavior at x = 0.5. There are several factors that affect the bowing parameter of solid solution materials including ionicity mismatch, crystal lattice mismatch, solubility, electron potential and electronegativity [13, 53, 59, 62].

4.1.1.1. Solubility

The solubility of a compound and its alloys can be directly linked to the amount of bowing that occurs in the band gap over composition range. Alloys which contain large

regions where spinodal decomposition would favour phase separation, tend to produce a larger bowing parameter than alloys with minimal or nonexistent miscibility gaps [63].

This is evident from pseudo-binary phase diagram of PbSe-PbTe in Figure 4.6 that a miscibility gap only occurs at low temperatures (T < 170) throughout the $(PbTe)_{(1-x)}(PbSe)_x$ compositions and full range solid solution present above 170 K. Hence, solubility factor has minimum influence on band gap bowing of $(PbTe)_{(1-x)}(PbSe)_x$ system. However, it might result in bowing of band gap for $(PbTe)_{0.9-y}(PbSe)_{0.1}(PbS)_y$ and $(PbTe)_{0.65-y}(PbSe)_{0.35}(PbS)_y$ systems as their alloys contain a sizeable miscibility gap (Figure 4.16).

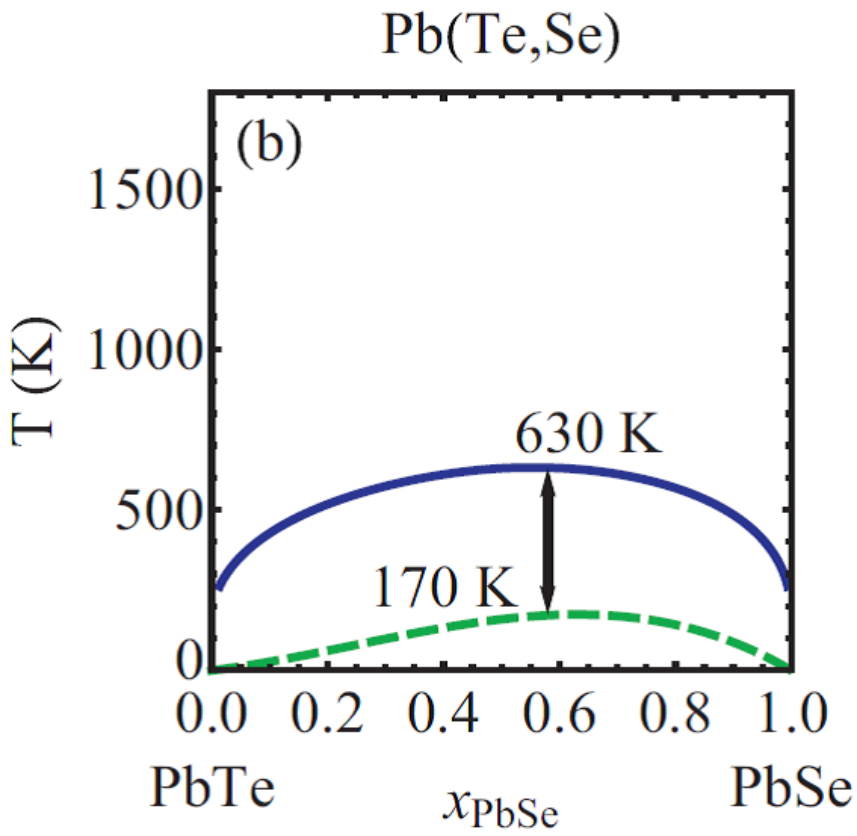

Figure 4.6: Ternary phase diagram for $PbSe_xTe_{1-x}$ showing the calculated incoherent miscibility gap (solid blue line) which is inflated from the vibrational enthalpy of mixing and experimental coherent miscibility gap (green dashed line) [64].

4.1.1.2. Atomic size and ionicity

The atomic size and ionicity mismatch of the atoms have shown to predominantly result in bowing of band gap in many similar solid solution systems [57, 61, 62, 65, 66]. In systems such as (Zn, Mg, Be)O, $BaTiO_3$-$CaTiO_3$, $BaTiO_3$-$BaZrO_3$, $SrTiO_3$-$BaZrO_3$ and $Mg_xZn_{1-x}Se$, there are large variations to the atomic size and ionicity of participant atoms, which were believed to be the cause for the band gap bowing. Table 4.1 shows the atomic size and ionic radius of the two components (PbSe and PbTe). Both phases have similar atomic radium and iconic values and hence it is unlikely that these factors play a major role in the observed bowing of the band gap in the $PbSe_xTe_{1-x}$ system.

4.1.1.3. Electronegativity

The electronegativity of individual anions bonded to the cations have also been pinpointed as a major component in determining the degree to which band gap bowing occurs in alloys [59]. The electronegativity values of Te, Se and S atoms are 2.10, 2.55 and 2.58 respectively using the Pauling scale. Similar to PbTe-PbSe system, Figure 4.7 demonstrates the electric charge of elements in CdTe–CdSe solid solution alloys. The electric charges of Cd, Te and Se provided in Figure 4.7 were calculated through the integration of the partial density of states (PDOS) until it reached the Fermi level. It is evident that in their pure states, Se atoms contain a higher electric charge and therefore higher electronegativity than Te atoms (2.55 > 2.10). However it has been shown that in their alloy states, the electronegativity of the Te atoms begin to increase while simultaneously the Se atoms electronegativity starts to decrease. This trend continues to occur until a point is reached where the electronegativity of both atoms reach similar charges, and it is at this point where the Te and Se atoms commence to compete over more charges than the other atom. This struggle to gain more charges results in the collected charges to build up on either Cd-Te or Cd-Se bonds and produces the characteristic bowing in the band gap [59]. The bowing parameter for $CdSe_xTe_{1-x}$ was calculated using Equation 4.1, where the band gaps were determined via the photoluminescence (PL) technique described in Chapter 2.

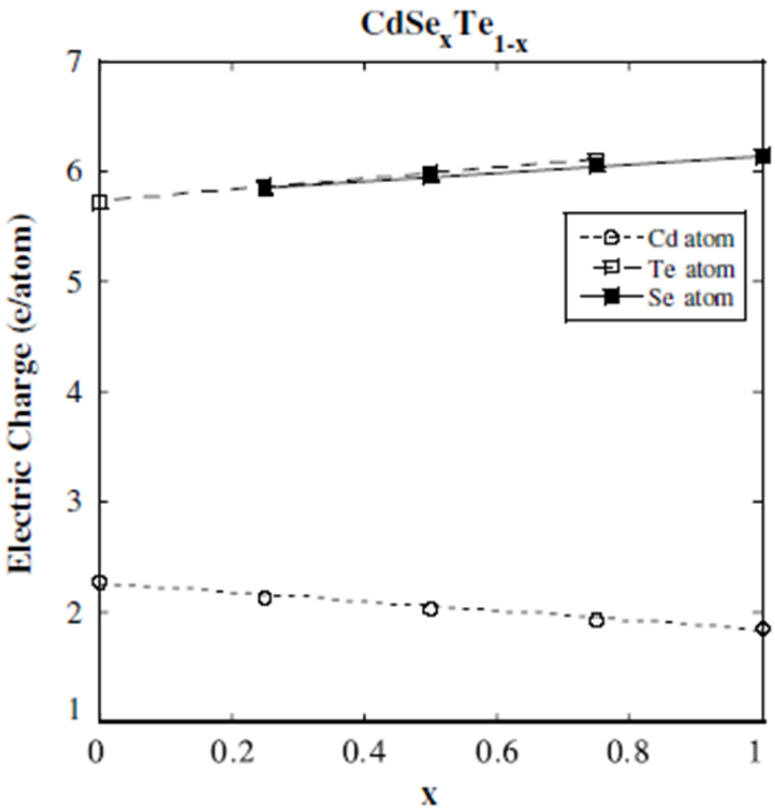

Figure 4.7: The variation in the electric charge of Te, Se and Cd atoms for the $CdSe_xTe_{1-x}$ compound with composition [59].

4.1.1.4. Valence Electron Potential

The final factor which, has been identified to play an integral role in the band gap bowing of alloys, is the effect of valence electron potential variation in the Te, Se and S atoms. The apparent bowing observed can be separated into two fundamental principles, achieved by the analysis of the alloying effect on the valence electron potential, through the use of the Schrödinger equation. The symmetric potential term represents the virtual crystal behavior of a semiconductor alloy AB as follow [63] :

$$\boldsymbol{U_s = \sum_{r'}[xU_A(r') + (1-x)U_B(r')]} \qquad 4.2$$

Where U_S is the symmetric potential term, U_A is the potential term of atom "A", U_B is the potential term of atom "B" and r is the particles position. This equation changes the valence electron potential for the material equivalent to that of the non-alloyed behavior as this term only accounts for the average changes to the valence electron

potential, rather than the localized changes to the core potential. The Schrödinger equation for this symmetric term can now be solved using the standard method since it is just the average potential that varies and the lattice symmetry remains constant.

However it is with the introduction of the asymmetric potential term that reveals how valence electron potential differences can result in band gap deviation. This term describes the non-uniform part of the valence electron potential:

$$\boldsymbol{U_a = \sum_{r'}[U_A(r' - \tau) - U_B(r' - \tau)]c_\tau} \qquad 4.3$$

Where U_a is the asymmetric potential term, U_A is the potential term of atom "A", U_B is the potential term of atom "B", $\boldsymbol{c_\tau}$ is the pair correlation function and $\boldsymbol{\tau}$ is the displacement of the atom at lattice site r. Here the valence electron potential for the alloy is dependent on the local variations as a result of compositional fluctuations. Solving of the Schrödinger equation becomes more difficult with this term as the lattice symmetry has been disrupted for this alloy due to the local defects associated with these changes to the core potential. This non uniformity is characterized by the addition of the pair correlation function ($\boldsymbol{c_\tau}$) to the asymmetric potential term. This value is determined by the probability of finding atom A rather than atom B at a known distance and direction from a chosen lattice site. This provides us with a good representation for the deviation of the alloy from the virtual crystal (non-alloyed) behavior, given by the symmetric term above. Therefore, the greater the difference in valence electron potential between two atoms, the larger the pair correlation function value. In turn, this produces a bigger separation from the virtual crystal behavior and a significant band gap bowing for this alloy.

For PbTe-PbSe system, the two atoms of importance are Te and Se which give corresponding valence electron potentials of 59 and 120 eV respectively. This value for the valence electron potential is an indication of the individual atoms reactivity and can be calculated using the equation [67]:

$$\boldsymbol{-eV = \frac{kn}{r}} \qquad 4.4$$

Where –eV is the valence electron potential, n is the number of valence electrons, r is the ionic radius (Å), and k is the proportionality factor used to convert Angstrom (Å) into centimetres (cm) and transform the force used by the valence electrons into electron volts (eV).

It is evident that Se atoms have double the electron potential of Te atoms so this particular alloy system should deviate significantly from the non-alloyed behavior. This is due to the pair correlation function returning a value that is quite large relative to the $(PbTe)_{0.9-y}(PbSe)_{0.1}(PbS)_y$ and $(PbTe)_{0.65-y}(PbSe)_{0.35}(PbS)_y$ systems.

4.1.2. Summary

Table 4.1 summarizes all factors that result in bowing of band gap in solid solution alloys of PbTe-PbSe. The solubility, atomic size and ionicity factors suggest a minimal band gap bowing for the ternary $(PbTe)_{(1-x)}(PbSe)_x$ system, whereas, the electron potential and electronegativity proposes a significant amount of the bowing in the $(PbTe)_{(1-x)}(PbSe)_x$ system. Therefore, it is reasonable to attribute the bowing parameter in this system to the difference in the valence electron potential and electronegativity of the Te and Se atoms.

Table 4.1: Different properties affecting bowing parameter of binary PbTe and PbSe lead chalcogenides.

	Ionic radius [68] (Å)	**Lattice constant (Å)[3]**	**Electronegativity (Pauling)[69]**	**Valence Electron potential (-eV)**	**Band Gap (eV)**
PbSe	1.98	6.12	2.55	120	0.27
PbTe	2.21	6.50	2.10	59	0.29

4.2. Quaternary $(PbTe)_{0.9-y}(PbSe)_{0.9}(PbS)_y$ system

Table 4.2 shows that the binary PbS compound has a much larger band gap (0.41 > 0.29 eV), valence electron potential (160 > 59 -eV) and electronegativity (2.58 > 2.10 Pauling) than analogous PbTe compound. While it has marginally smaller lattice constant (5.94 < 6.50 Å) and ionic radius (1.84 < 2.21 Å). In this section and the

following one, PbS is added to the ternary $(PbTe)_{(1-x)}(PbSe)_x$ system to fabricate quaternary $(PbTe)_{1-x-y}(PbSe)_x(PbS)_y$ alloys in order to study the variation of band gap as a function of PbS content.

Table 4.2: Different properties affecting bowing parameter of binary PbTe, PbSe and PbS lead chalcogenides.

	Ionic radius [68] (Å)	**Lattice constant (Å)[3]**	**Electronegativity (Pauling)[69]**	**Valence Electron potential (-eV)**	**Band Gap (eV)**
PbS	1.84	5.94	2.58	160	0.41
PbSe	1.98	6.12	2.55	120	0.27
PbTe	2.21	6.50	2.10	59	0.29

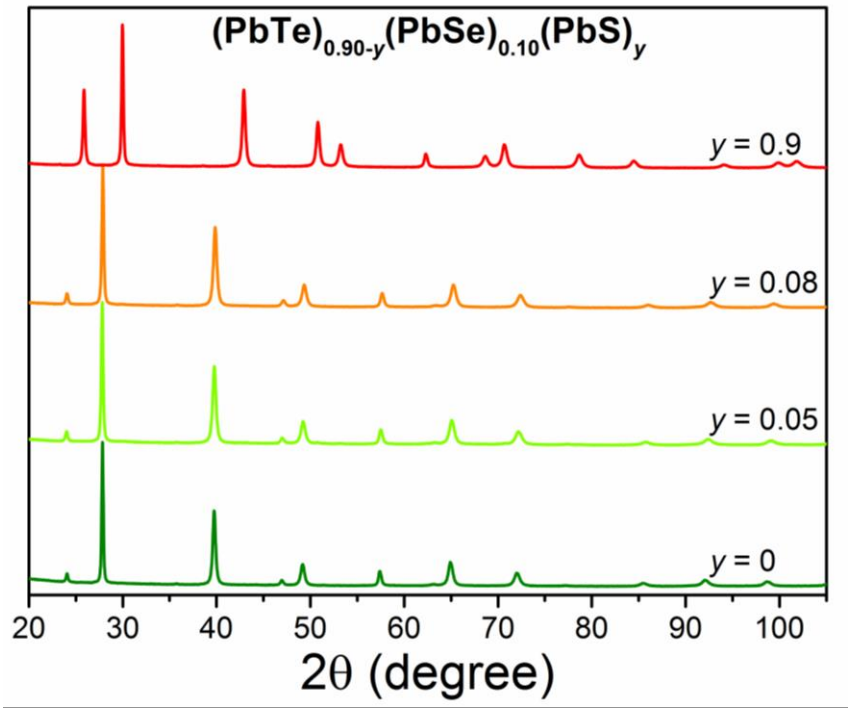

Figure 4.8: Powder X-ray diffraction patterns for quaternary $(PbTe)_{0.9-y}(PbSe)_{0.1}(PbS)_y$ system.

Figure 4.8 shows the XRD patterns obtained from quaternary samples of $(PbTe)_{0.9-y}(PbSe)_{0.1}(PbS)_y$ (y = 0, 0.05, 0.08 and 0.9). This particular set of samples were chosen

to elucidate the effect of PbS addition on the band gap of ternary solid solution $(PbTe)_{0.9}(PbSe)_{0.1}$ alloys. The introduction of PbS to the ternary $(PbTe)_{(1-x)}(PbSe)_x$ system and obtaining single phase alloys is a challenging procedure. The solubility of PbS in PbTe binary system is very limited due to a large miscibility gap between PbTe and PbS phases where the two-phase compounds would occur [70]. Secondary phase of PbS precipitate within PbTe matrix at concentrations as low as 4 at% [71]. The quaternary phase diagram shown in Figure 4.13 indicates that the composition regions in which single phase solid solution can be fabricated are limited. The single phase sample is vital in obtaining an accurate band gap measurement as it has been shown that for some semiconductors the appearance of two phases results in an inflated band gap energy [16]. Hence the chosen compositions for measurement should lie outside this dual phase region where only single phase alloys can be obtained. Presence of PbSe in quaternary compounds of $(PbTe)_{0.9-y}(PbSe)_{0.1}(PbS)_y$ has shown to increase PbS solubility in ternary alloy of $(PbTe)_{0.9}(PbSe)_{0.1}$ [56, 72]. However, it is not clear to what extend the PbS content effects on the band gap of alloys.

Quaternary samples of $(PbTe)_{0.9-y}(PbSe)_{0.1}(PbS)_y$ (y = 0, 0.05, 0.08 and 0.9) can be identified as single phase compounds since no additional peaks is detected in XRD patterns of Figure 4.8. Figure 4.8 not only validates the singular phase of the these samples, but also shows the progressive shift of peaks to higher 2theta values as the lead telluride content is reduced from 90% to 0%. This phenomenon can be explained by the smaller Selenium and Sulphur atoms, 120 pm and 100 pm respectively, replacing the larger Tellurium atoms, 140 pm, as a result of solid solution alloying. This effect becomes increasingly evident at the higher angles (>80) and can be more thoroughly comprehended by understanding Bragg's Law (Equation 3.1) and how the atomic spacing (d) of an atom can affect the angle (2Theta).

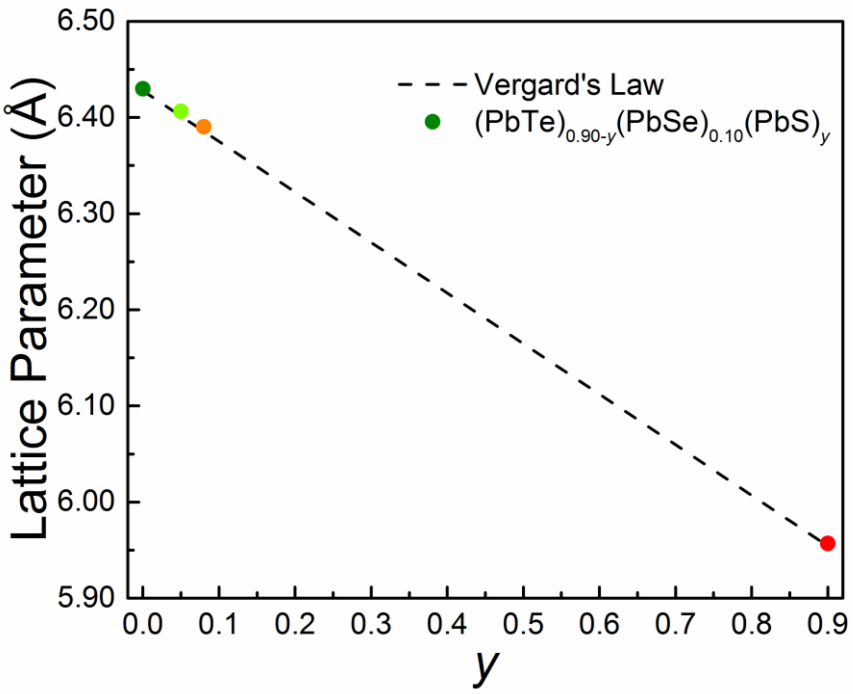

Figure 4.9: Lattice Parameters of quaternary $(PbTe)_{0.9-y}(PbSe)_{0.1}(PbS)_y$ system as a function of composition.

Rietveld analysis was implemented on the X-ray diffraction patterns from Figure 4.8 in order to calculate the lattice parameters (summarised in Figure 4.9). The change in lattice parameter with PbS content follows Vergard's Law, indicating single phase solid solution alloys.

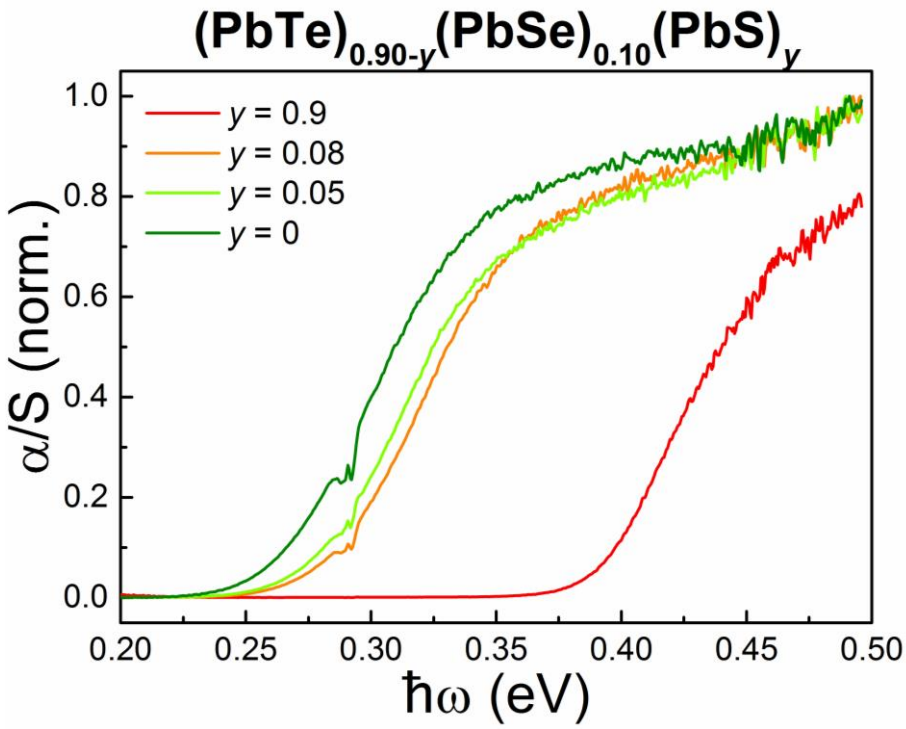

Figure 4.10: Normalized Kubelka Munk transformations for quaternary $(PbTe)_{0.9-y}(PbSe)_{0.1}(PbS)_y$ system from raw data obtained using DRIFT spectroscopy.

The absorption edge spectra has been measured at room temperature for the $(PbTe)_{0.9-y}(PbSe)_{0.1}(PbS)_y$ series through the Diffuse Reflectance Infrared Fourier Transform (DRIFT) technique. Figure 4.10 shows the transformation from the raw data produced using Fourier Transform Infrared (FTIR) spectroscopy to the normalized α/S ratio using Kubelka Munk theory. The shift in energy to a higher value with increasing Sulphur content is evident. This trend differs to that of the $(PbTe)_{(1-x)}(PbSe)_x$ system due to the addition of PbS to the compound in the $(PbTe)_{0.9-y}(PbSe)_{0.1}(PbS)_y$ system. The band gap energy of PbS is much higher (0.41 eV) than that of PbSe (0.27 eV) and PbTe (0.29 eV), hence this difference in the energy gap between the PbS-free sample of $(PbTe)_{0.9}(PbSe)_{0.1}$ and PbTe-free $(PbSe)_{0.1}(PbS)_{0.9}$ sample, results in a larger energy range for the measurements to spread across. This difference can be visualized by comparing the cluttering of Figure 4.3 where the energy difference is 0.02 eV and Figure 4.10 where the samples are much more spaced with an energy difference of 0.11 eV.

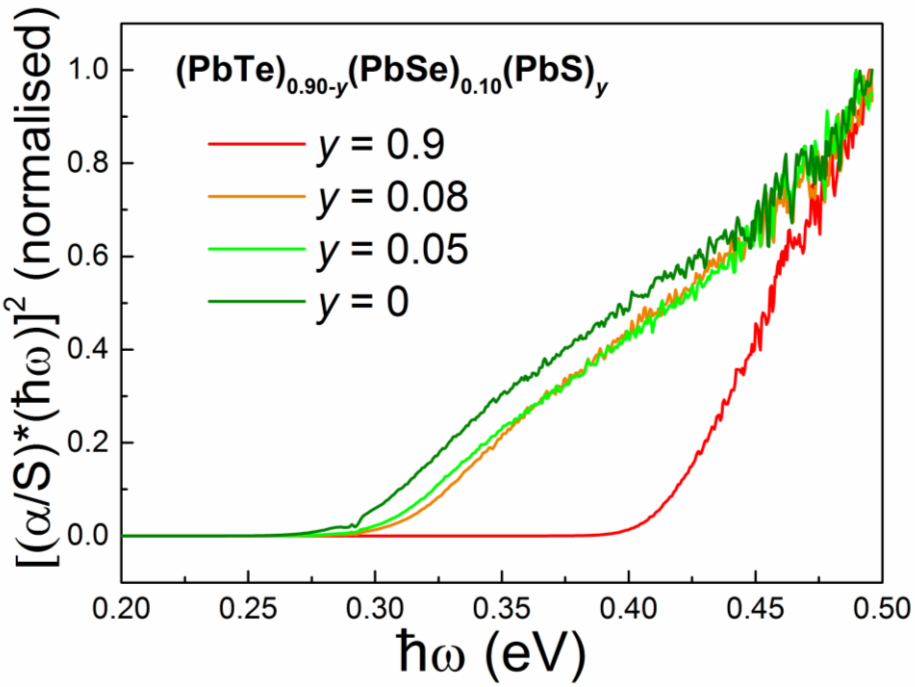

Figure 4.11: Normalized Kubelka Munk transformations for quaternary $(PbTe)_{0.9-y}(PbSe)_{0.1}(PbS)_y$ system from the application of Tauc method for direct gaps.

By applying the Tauc method transformations (Equation 2.7) for direct band gaps to Figure 4.10, the band gap energies for the $(PbTe)_{0.9-y}(PbSe)_{0.1}(PbS)_y$ series can be calculated from the normalized Kubelka Munk graph, shown in Figure 4.11. This is achieved through identifying the linear section of the each curve, followed by the extrapolation of this linear section to the baseline where the direct band gap of that sample is determined.

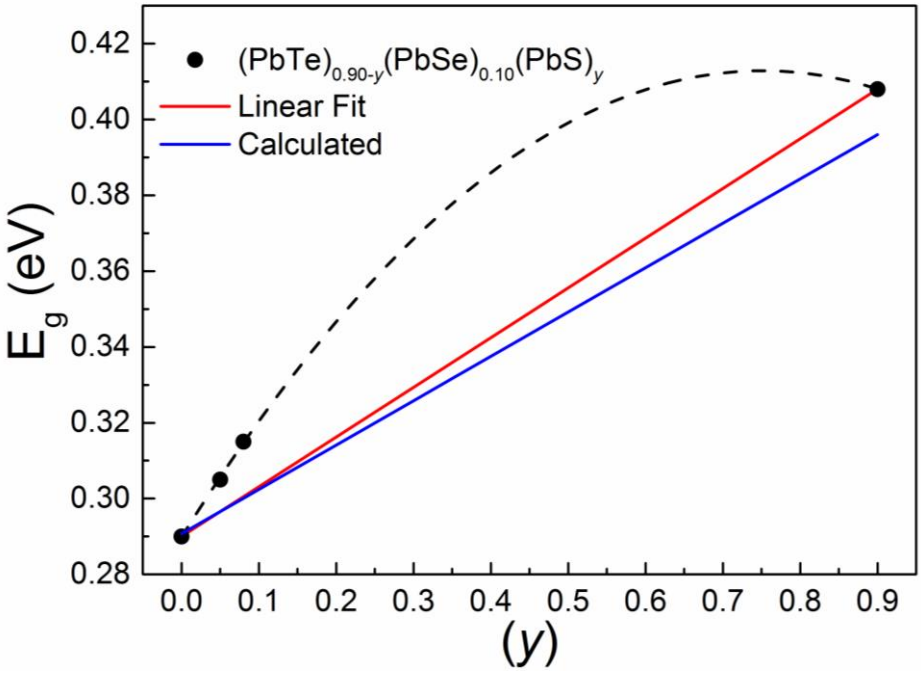

Figure 4.12: The direct band gaps for quaternary $(PbTe)_{0.9-y}(PbSe)_{0.1}(PbS)_y$ system as a function of PbS concentration.

Figure 4.12 shows the calculated, linear assumption and measured variation of direct band gap energy with increasing PbS content for quaternary $(PbTe)_{0.9-y}(PbSe)_{0.1}(PbS)_y$ system. The calculated curve is a linear prediction of the band gap using the band gap measured for the pure binary compounds of PbTe, PbSe and PbS. The linear assumption curve in Figure 4.12 is the predicted linear variation in band gaps with composition between the ternary alloys of PbTe-free $(PbSe)_{0.1}(PbS)_{0.9}$ and PbS-free $(PbTe)_{0.9}(PbSe)_{0.1}$. This is commonly regarded as the most accepted and expected result for single phase solid solution alloys. The third curve (Figure 4.12) connects the measured band gap values achieved through experimental procedures for the single phase samples, fitted with the parabolic equation. In the above section, it is discussed that at x > 0.09, PbS secondary phase precipitates within PbTe matrix. Therefore, this hypothetical curve is dashed in Figure 4.12. However, it is evident that, similar to the ternary $(PbTe)_{(1-x)}(PbSe)_x$ system, the band gaps of these quaternary samples also deviate from the predicted linear fit and illustrates the bowing effect which is explained by the parabolic polynomial equation [60]:

$$E_{g,PbTeSeS} = xE_{g,PbSe0.1S0.9} + (1-x)E_{g,PbSe0.1Te0.9} - bx(1-x) \qquad 4.5$$

4.3. Quaternary $(PbTe)_{0.65-y}(PbSe)_{0.35}(PbS)_y$ system

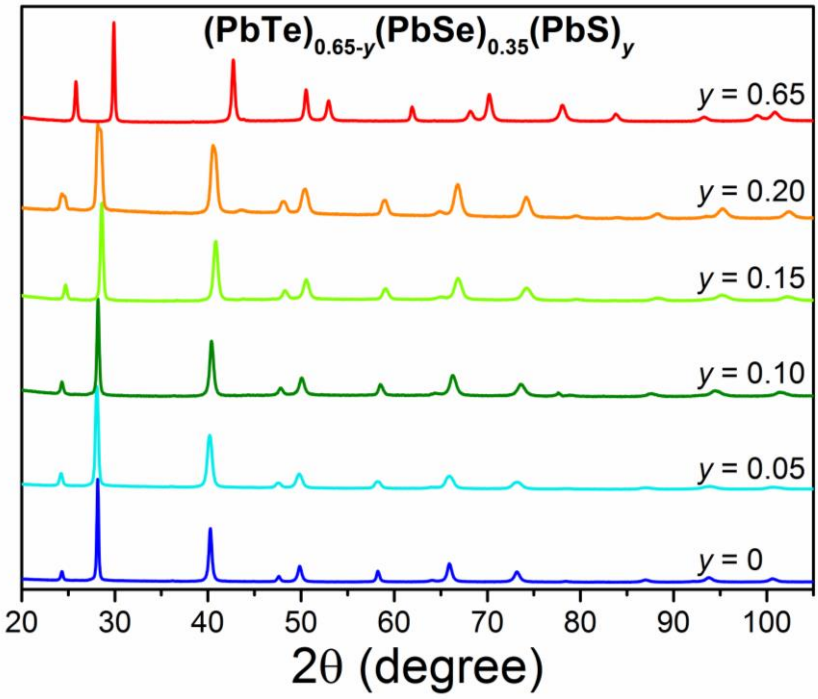

Figure 4.13: Powder X-ray diffraction patterns for quaternary $(PbTe)_{0.65-y}(PbSe)_{0.35}(PbS)_y$ system.

Figure 4.13 shows the XRD patterns for the quaternary $(PbTe)_{0.65-y}(PbSe)_{0.35}(PbS)_y$ system, (y = 0, 0.05, 0.10, 0.15, 0.20 and 0.65). Figure 4.14 clearly shows each sample only contains peaks of a single phase compound and no additional peaks have been detected.

The slight shift in 2theta values of peaks, which becomes more pronounced at higher angles, is observed with increase of PbS content. The larger Tellurium atoms (140 pm) are replaced with the smaller Sulphur atoms (100 pm) similar to previous $(PbTe)_{0.9-y}(PbSe)_{0.1}(PbS)_y$ system.

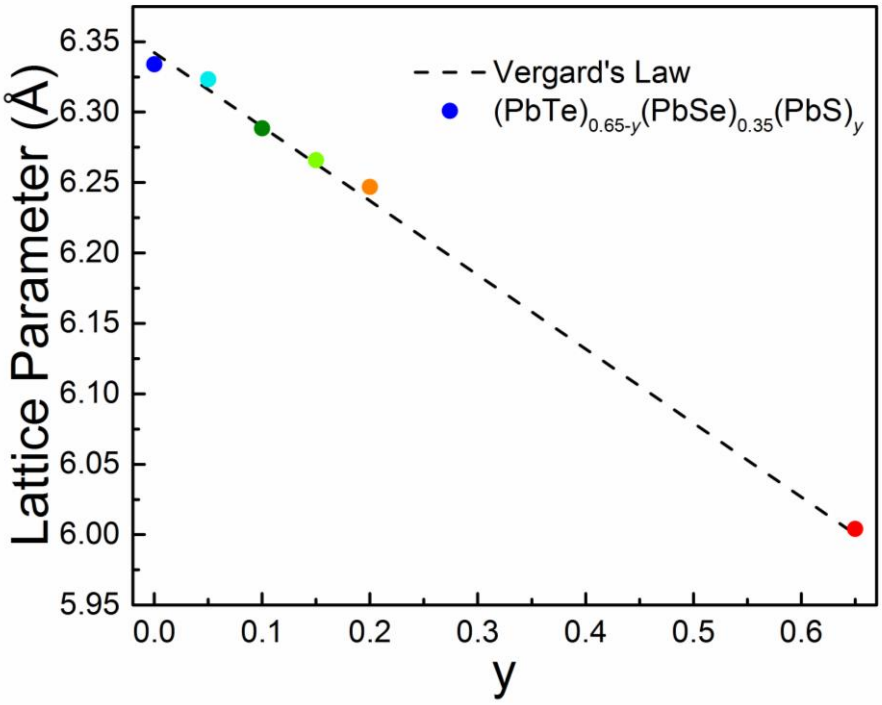

Figure 4.14: Lattice Parameters for quaternary $(PbTe)_{0.65-y}(PbSe)_{0.35}(PbS)_y$ system as a function of PbS content.

Following the Rietveld refinement to the X-ray diffraction pattern of individual samples in Figure 4.13, the lattice parameters were determined and plotted against the composition in Figure 4.14. Having pinpointed the predicted single phase compounds from the $(PbTe)_{0.65-y}(PbSe)_{0.35}(PbS)_y$ quaternary phase diagram in Figure 4.18 it can be definitively stated that these compounds are all in fact single phase. The miscibility gap shown by the phase diagram in Figure 4.18 is the reason for the significant gap in samples between y=0.20 and y = 0.65 where two phase compounds would likely have occurred. The fabricated samples can be labeled as single phase since all data points lie on the straight line plotted in Figure 4.14, which follows Vergard's Law.

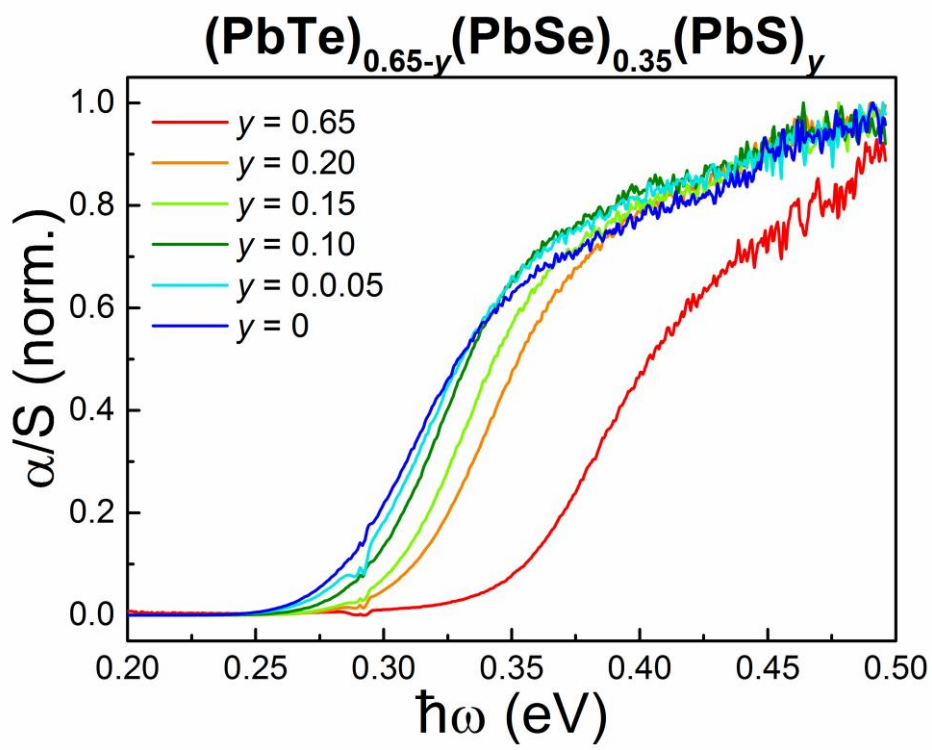

Figure 4.15: Normalized Kubelka Munk transformations for quaternary $(PbTe)_{0.65-y}(PbSe)_{0.35}(PbS)_y$ system from raw data obtained using DRIFT spectroscopy.

The absorption data of each sample in the $(PbTe)_{0.65-y}(PbSe)_{0.35}(PbS)_y$ system is measured at room temperature using FTIR equipment. It is evident from Figure 4.15 that there is an increase in energy across the six samples, with a slight shift occurring from y=0 to y=0.20, then a significant increase for y=0.65. This progressive increase in energy is due to the replacement of the lower energy PbTe (0.29) with the higher energy PbS (0.41). There is only a relatively small increase in energy gap when y is increases by 0.05 and a larger variation occurs when it further increase to 0.65.

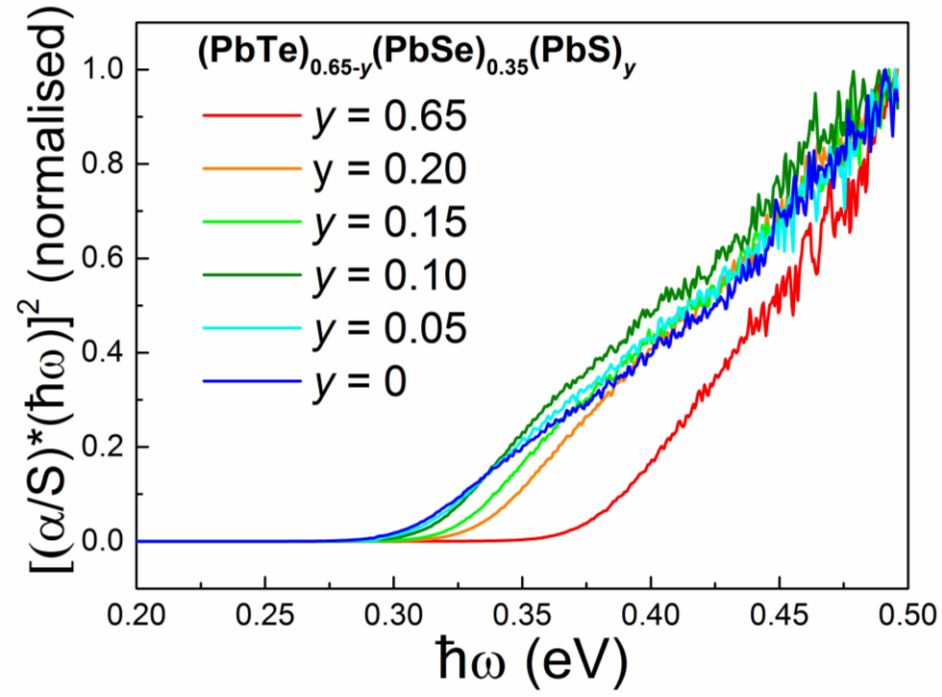

Figure 4.16: Normalized Kubelka Munk transformations for quaternary $(PbTe)_{0.65-y}(PbSe)_{0.35}(PbS)_y$ system from the application of Tauc method for direct gaps.

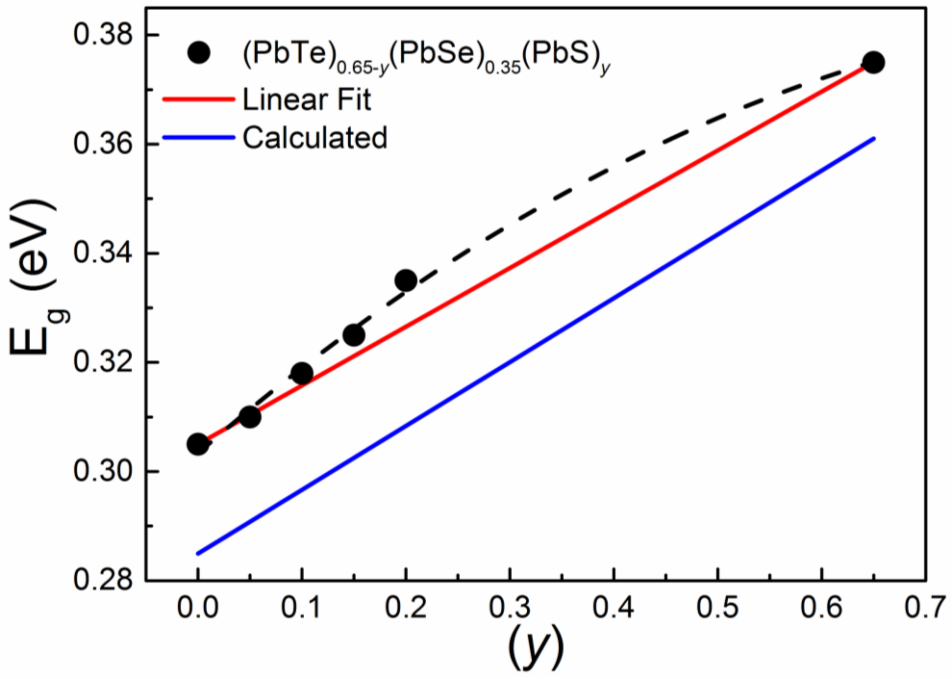

Figure 4.17: The direct band gaps quaternary $(PbTe)_{0.65-y}(PbSe)_{0.35}(PbS)_y$ system as a function of PbS concentration.

Figure 4.17 shows the calculated, linear assumption and measured curves of the band gap determined for quaternary $(PbTe)_{0.65-y}(PbSe)_{0.35}(PbS)_y$ samples, indicating the

variation of direct band gap energy versus PbS content for quaternary $(PbTe)_{0.65-y}(PbSe)_{0.35}(PbS)_y$ system. The calculated curve is a linear prediction of the band gap using the band gap measured for the pure binary compounds of PbTe, PbSe and PbS. The linear assumption curve in Figure 4.17 is the predicted linear variation in band gaps with composition between the ternary alloys of PbTe-free $(PbSe)_{0.35}(PbS)_{0.65}$ and PbS-free $(PbTe)_{0.65}(PbSe)_{0.35}$.

The experimental data deviate slightly from linear relationship. The calculated curve for $(PbTe)_{0.65-y}(PbSe)_{0.35}(PbS)_y$ compounds shows band gaps much less than the linear assumption and experimental data, due to the smaller band gap value obtained for binary PbSe, PbTe and PbS using the literature (Table 2.1) compared with the values obtained experimentally.

4.3.1. Quaternary Band Gap Bowing

The bowing parameter (b) for quaternary $(PbTe)_{0.9-y}(PbSe)_{0.1}(PbS)_y$ system is calculated to be -0.21813 ± 0.01561 eV. Because the parabola is inverted compared to a normal parabola, the negative value is obtained for the bowing parameter [63] . The bowing parameter for quaternary $(PbTe)_{0.9-y}(PbSe)_{0.1}(PbS)_y$ system (-0.21813 ± 0.01561 eV) is larger than bowing parameter for ternary $(PbTe)_{1-x}(PbSe)_x$ system (-0.052 ± 0.011 eV). The bowing parameter is influenced by factors such as ionicity mismatch, crystal lattice mismatch, solubility, electron potential and electronegativity. These factors will be explored below.

The bowing parameter (b) for quaternary $(PbTe)_{0.65-y}(PbSe)_{0.35}(PbS)_y$ system is calculated to be -0.08326 ± 0.02352 eV using the procedure described in details in Section 4.1. The bowing parameter of this system (-0.08326 eV) is much smaller than the one for quaternary $(PbTe)_{0.9-y}(PbSe)_{0.1}(PbS)_y$ system (-0.21813 eV) and larger than -0.052 eV for ternary system of $(PbTe)_{(1-x)}(PbS)_x$.

4.3.1.1. Solubility

The larger the extend of the solubility is for two compounds, the smaller is the degree to which the bowing deviates from the linear relationship [63]. The ternary $(PbTe)_{1-x}(PbSe)_x$ system shows unlimited solubility over the composition range, whereas there is a sizeable miscibility gap exists between PbTe and PbS compounds (Figure 4.13). This explains a larger bowing parameter present for the quaternary $(PbTe)_{0.9-y}(PbSe)_{0.1}(PbS)_y$ system compared to the ternary $(PbTe)_{1-x}(PbSe)_x$.

Alloys with a larger miscibility gap in the phase diagram show larger bowing parameter (b) [59]. This has shown to be the major contributor in band gap bowing of quaternary $(PbTe)_{0.9-y}(PbSe)_{0.1}(PbS)_y$ system, where there is a large miscibility gap (green curve in Figure 4.18) existed between ternary phases of $(PbTe)_{0.9}(PbSe)_{0.1}$ and $(PbSe)_{0.1}(PbS)_{0.9}$ whereas, the size of miscibility gap for the $(PbTe)_{0.65-y}(PbSe)_{0.35}(PbS)_y$ system is much smaller (yellow curve in Figure 4.18). Therefore one would expect to see a larger bowing parameter for the $(PbTe)_{0.9-y}(PbSe)_{0.1}(PbS)_y$ system due to its reduced miscibility gap compared to the $(PbTe)_{0.65-y}(PbSe)_{0.35}(PbS)_y$ system. Both quaternary systems show larger bowing parameters than ternary $(PbTe)_{1-x}(PbSe)_x$ with complete solubility over composition range.

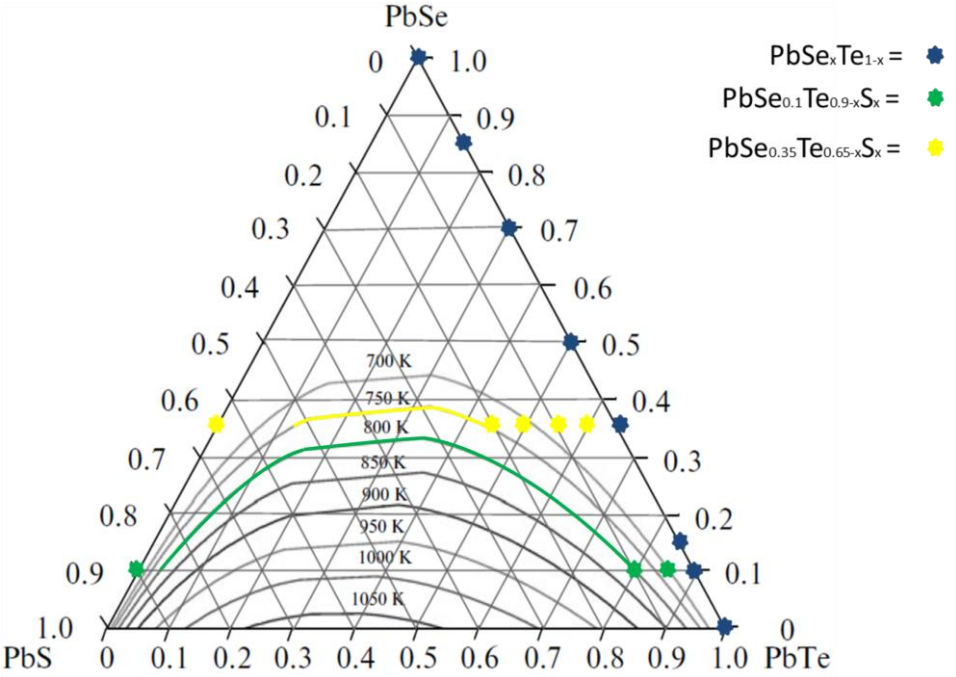

Figure 4.18: The quaternary phase diagram for PbSe-PbTe-PbS identifying the large miscibility gap for the $(PbTe)_{0.9-y}(PbSe)_{0.1}(PbS)_y$ system (adapted from [17]).

4.3.1.2. Atomic Size and Ionicity

The introduction of the PbS compound creates a slightly larger lattice and ionic mismatch for the $(PbTe)_{0.9-y}(PbSe)_{0.1}(PbS)_y$ system compared to the ternary $(PbTe_{)(1-x)}(PbS)_x$ system. The figures from Table 4.2 support that replacing the larger Te atom with the smaller S atom produces a larger mismatch, which in turn increases the bowing parameter [62].

4.3.1.3. Electronegativity

The electronegativity effect is used to measure an atoms ability to draw electrons from surrounding atoms toward itself. The electronegativity of an atom is determined by its atomic number and how far the outer electrons lie from the inner nucleus. The Pauling scale is the most frequently used method to compare electronegativity's, where Fluorine is given the highest value of 4.0 and this value decreases down through all the elements to Caesium and Francium at 0.7[69]. It should be possible to predict the degree to which band gap bowing occurs in the pseudo ternary lead chalcogenide systems, through investigating the electronegativity of each individual ionic bond to

the central Pb atom. The electronegativity values of Te, Se and S ions are 2.10, 2.55 and 2.58 respectively according to the Pauling scale. As discussed in Section 4.1 where only PbTe and PbSe bonds were present in the ternary $(PbTe)_{(1-x)}(PbS)_x$ system, the band gap bowing was attributed to the Se ions having higher electronegativity compared to the Te ions (2.55 > 2.10). However, addition of the S ions further increases electronegativity (2.58) in the quaternary $(PbTe)_{0.9-y}(PbSe)_{0.1}(PbS)_y$ system. It is therefore expected that the bowing parameter for these compounds to rise above that of the ternary $(PbTe_{)(1-x)}(PbS)_x$ system.

Similar to the $(PbTe)_{0.9-y}(PbSe)_{0.1}(PbS)_y$ system, the introduction of the S ions replacing the Te ions bonding to the central Pb atom in the $(PbTe)_{0.65-y}(PbSe)_{0.35}(PbS)_y$ compound results in a larger disparity of electric charge for this system (2.58 > 2.10). Furthermore, it is possible to distinguish two quaternary systems containing PbS by comparing the quantity of S and Se ionic bonds with the number of Te ionic bonds. It is evident that the $(PbTe)_{0.9-y}(PbSe)_{0.1}(PbS)_y$ system contains less S ionic bonds due the composition in the series only reaching 8% PbS. In comparison to the $(PbTe)_{0.65-y}(PbSe)_{0.35}PbS)_y$ system where the PbS content is able to reach 20%. Therefore we should expect a smaller contribution from the electronegativity to the bowing parameter for this compound than Section 4.2.

4.3.1.4. Valence Electron Potential

Similar to the electronegativity, differing valence electron potentials of the individual atoms in a specific system has also been pinpointed as having a significant effect on the band gap bowing in that system. As discussed in Section 4.1, a recent study shows how the bowing parameter can be split into two fundamental principles through analyzing the alloying effect on this valence electron potential with the application of the Schr**ö**dinger equation [63] . It was discovered that a larger pair correlation function value (c_τ) was produced from compounds containing atoms of greater variation in valence electron potential. Hence, more bowing in the band gap data is anticipated for this compound.

For the quaternary $(PbTe)_{0.9-y}(PbSe)_{0.1}(PbS)_y$ system, the valence electron potentials of

the three atoms of significance are 59, 120 and 160 -eV for Te, Se and S respectively. From first glance it is obvious that the valence electron potentials increase significantly from Te to Se to S. This large difference in valence electron potentials suggests that these alloyed compounds should deviate from the traditionally accepted linear non-alloyed behavior. The quaternary $(PbTe)_{0.9-y}(PbSe)_{0.1}(PbS)_y$ system presented a larger bowing parameter compared to the ternary $(PbTe_{)(1-x)}(PbS)_x$ compounds (-0.218 > -0.052 eV). This is predominantly due to the valence electron potential of the S atom being more than two and half times the valence electron potential of the Te atom. By introducing S atoms into the compound it is proven that this noticeably has increased the band gap deviation from the linear prediction.

The amount of PbSe remains constant at 35% for all compounds of $(PbTe)_{0.65-y}(PbSe)_{0.35}(PbS)_y$ system and PbTe is replaced with PbS. Table 4.2 clearly shows the valence electron potential of PbS is much higher than PbTe (160 > 59 eV), suggesting an increase in the pair correlation function (c_τ) and increased deviation from the non-alloyed behavior [63]. Therefore, one would expect the $(PbTe)_{0.9-y}(PbSe)_{0.1}(PbS)_y$ system to show a larger bowing parameter than the $(PbTe)_{0.65-y}(PbSe)_{0.35}(PbS)_y$ compound due to the inflated PbS content at maximum composition (0.90 > 0.65). This expectation translates to the recorded experimental data as the bowing parameter for this $(PbTe)_{0.65-y}(PbSe)_{0.35}(PbS)_y$ series, returned a much lower value than the $(PbTe)_{0.9-y}(PbSe)_{0.1}(PbS)_y$ series from Section 4.2.

4.3.2. Summary

In conclusion, the investigation of all the factors influence the bowing parameter in solid solution alloys, suggest an increased band gap bowing parameter in the quaternary $(PbTe)_{0.9-y}(PbSe)_{0.1}(PbS)_y$ system compared to the ternary $(PbTe)_{(1-x)}(PbS)_x$ system. This hypothesis is supported by the data provided in Sections 4.1 and 4.2, most notably the band gap parameter for each system calculated using in Equations 4.1 and 4.5. The atomic size and chemical ionicity appear likely to be factors for the band gap bowing, as the lattice constant and ionic radius of PbS is marginally smaller than that of PbSe and PbTe. However more interestingly in the $(PbTe)_{0.9-y}(PbSe)_{0.1}(PbS)_y$ system,

the addition of the PbS compound appears to repeatedly stand out as the main reason for increased band gap bowing as it led to larger differences in the electronegativity and electron potential of the individual atoms.

In the following section, the band gap of quaternary $(PbTe)_{0.65-y}(PbSe)_{0.35}(PbS)_y$ system will be measured. The higher concentration of PbSe increases the solubility limit of PbS compared to $(PbTe)_{1-x-y}(PbSe)_x(PbS)_y$ system. According to the above discussion, it is anticipated that $(PbTe)_{0.65-y}(PbSe)_{0.35}(PbS)_y$ system shows a higher bowing parameter than the ternary $(PbTe)_{(1-x)}(PbS)_x$ system. The importance of the next section however, is to determine how much the bowing parameter is increased and compare it to the value determined for the $(PbTe)_{0.9-y}(PbSe)_{0.1}(PbS)_y$ compound in this section.

The addition of the PbS compound to this lead chalcogenide system, is increased both the total band gap and bowing parameter of $(PbTe)_{0.65-y}(PbSe)_{0.35}(PbS)_y$ compounds. Similar to Section 4.2 and the $(PbTe)_{0.9-y}(PbSe)_{0.1}(PbS)_y$ system, the increased disparity in values for the electronegativity and valence electron potential of the atoms seems to be the major factor in altering the bowing parameter value. A potential reason for the reduced bowing parameter in this system compared to $(PbTe)_{0.9-y}(PbSe)_{0.1}(PbS)_y$ system is the maximum amount of PbS content that can be incorporated in each series on the PbS-rich side of the compounds. The $(PbTe)_{0.65-y}(PbSe)_{0.35}(PbS)_y$ system can only contain 65% PbS and $(PbTe)_{0.9-y}(PbSe)_{o.1}(PbS)_y$ reaches 90% PbS, means less PbS atoms are present at this system and therefore a smaller difference in electronegativity and electron potential is obtained and consequently results in a smaller bowing parameter.

Chapter 5

Electronic transport Properties of Lead Chalcogenide Alloys

This chapter summarizes the room temperature Seebeck coefficient (S) and electrical resistivity (σ) of the quaternary $(PbTe)_{0.9-y}(PbSe)_{0.1}(PbS)_y$ and $(PbTe)_{0.65-y}(PbSe)_{0.35}(PbS)_y$ systems.

The thermal conductivity of $PbSe_{0.1}Te_{0.9}$, $PbSe_{0.1}S_{0.9}$ and $PbSe_{0.35}S_{0.65}$ samples are also measured using the laser flash method described in Chapter 3. These data have been used to describe the effect of band gap on bipolar effect observed for narrow band gap lead chalcogenides.

5.1. Room Temperature Seebeck and Resistivity

Table 5.1 summarizes the room temperature Seebeck and resistivity measurements for the $(PbTe)_{0.9-y}(PbSe)_{0.1}(PbS)_y$ and $(PbTe)_{0.65-y}(PbSe)_{0.35}(PbS)_y$ systems. The PbTe-free samples show negative Seebeck coefficient values, indicating intrinsically n-type semiconductor at room temperature, whereas, the rest of samples have positive room temperature Seebeck coefficient, demonstrating p-type semiconducting behaviour. All samples present high electrical resistivities due to the intrinsic nature of these samples compared to doped samples [21, 30, 73, 74]. Extrinsically doped samples produce a much smaller resistivity due to the increased number of electrons (n-type) or holes (p-type) available to be excited to the conduction band.

Extrinsically doped *n*-type [73, 75-77] and *p*-type [30, 55, 56] lead chalcogenides show room temperature resistivity values below 0.8 mΩ.cm [78], whereas the current study samples show resistivities between 6 to 90 mΩ.cm. Nevertheless, Gibbs [15] measured the optical band gaps for n-type $PbTe_{1-x}I_x$ series, showing that an increase in band gap

energy due to Burstein-Moss shift only begins to occur in heavily doped samples with carrier concentrations above 10^{19} cm^{-3} [15], indicating that the current study samples with high resistivities and low carrier concentrations would be hardly affected by the Burstein-Moss effect.

Table 5.1: The room temperature Seebeck and resistivity measurements for the $(PbTe)_{0.9-y}(PbSe)_{0.1}(PbS)_y$ and $(PbTe)_{0.65-y}(PbSe)_{0.35}(PbS)_y$ systems.

Sample	**Seebeck (μV.K^{-1})**	**Resistivity (mΩ.cm)**
$PbSe_{0.1}Te_{0.9}$	215	15
$PbSe_{0.1}S_{0.05}Te_{0.85}$	283	12
$PbSe_{0.1}S_{0.08}Te_{0.82}$	283	7
$PbSe_{0.1}S_{0.9}$	-233	6
$PbSe_{0.35}Te_{0.65}$	373	84
$PbSe_{0.35}S_{0.65}$	-201	5
$PbSe_{0.35}S_{0.05}Te_{0.6}$	330	89
$PbSe_{0.35}S_{0.1}Te_{0.55}$	313	85
$PbSe_{0.35}S_{0.15}Te_{0.5}$	250	80
$PbSe_{0.35}S_{0.2}Te_{0.45}$	220	70

It is evident that the largest discrepancies in electrical resistivity for the $(PbTe)_{0.9-y}(PbSe)_{0.1}(PbS)_y$ and $(PbTe)_{0.65-y}(PbSe)_{0.35}(PbS)_y$ systems occurs for PbTe-rich alloys, where the samples contain a higher PbTe content. As the PbS concentration is increased, the resistivity reduces until a minimum value of approximately 5 mΩ.cm is obtained for PbTe-free compounds. The relationship between these room temperature Seebeck and resistivity results and their significance will be discussed later in this chapter.

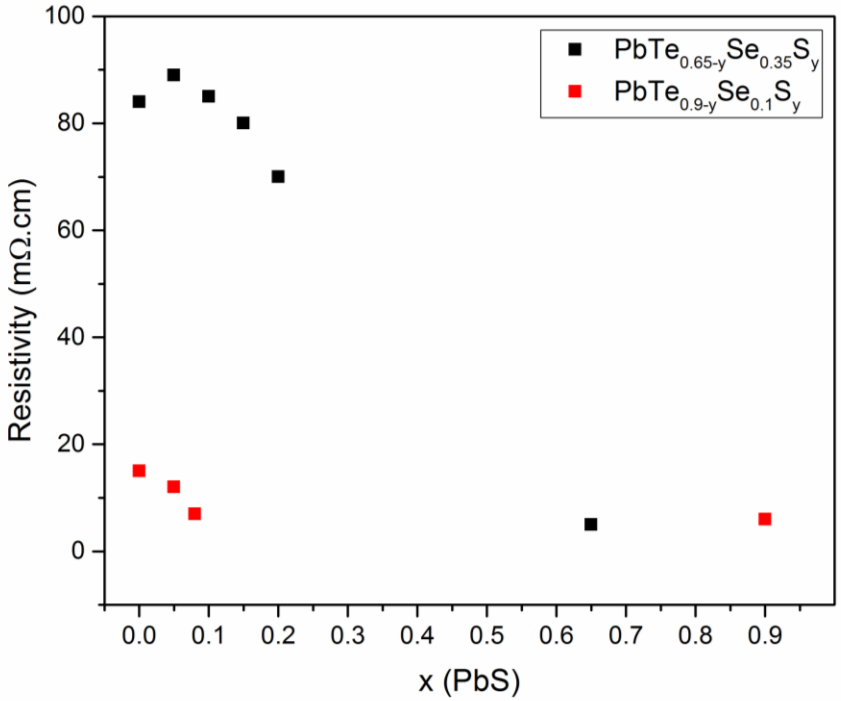

Figure 5.1: Room temperature electrical resistivity of $(PbTe)_{0.9-y}(PbSe)_{0.1}(PbS)_y$ and $(PbTe)_{0.65-y}(PbSe)_{0.35}(PbS)_y$ systems as a function of PbS content.

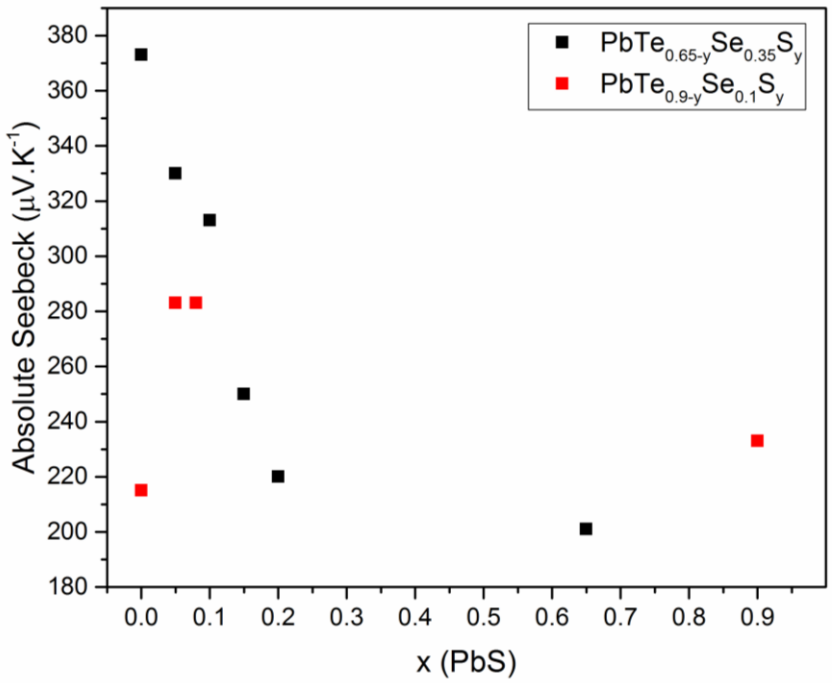

Figure 5.2: Room temperature absolute Seebeck measurements plotted against the PbS content for $(PbTe)_{0.9-y}(PbSe)_{0.1}(PbS)_y$ and $(PbTe)_{0.65-y}(PbSe)_{0.35}(PbS)_y$ systems.

5.2. Thermal Conductivity Measurements

The thermal conductivity of $PbSe_{0.1}Te_{0.9}$, $PbSe_{0.1}S_{0.9}$ and $PbSe_{0.35}S_{0.65}$ measured using LFA. These samples show energy gaps of 0.290, 0.408 and 0.375 eV respectively. The thermal conductivity results will be assessed to determine the magnitude of bipolar effect for these compounds with different band gap energy.

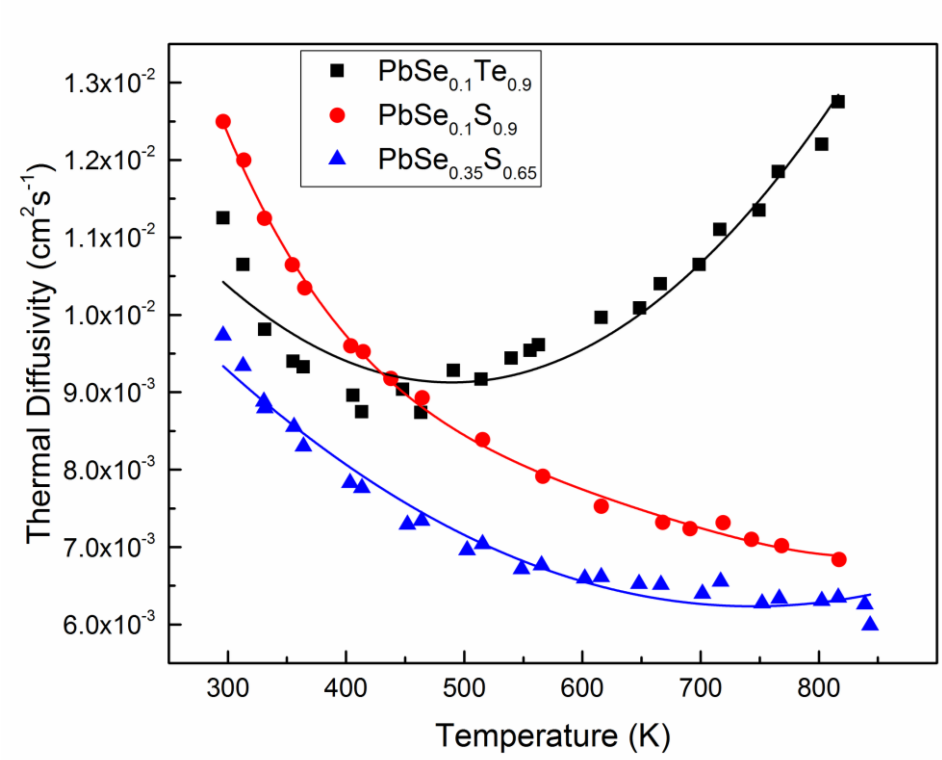

Figure 5.3: The measured thermal diffusivity for $PbSe_{0.1}Te_{0.9}$, $PbSe_{0.1}S_{0.9}$ and $PbSe_{0.35}S_{0.65}$ as a function of temperature.

The measured thermal diffusivity (D_T) of each sample as a function of temperature is shown in Figure 5.3. The temperature dependent calculated specific heat capacities of samples are shown in Figure 5.4. In order to transform the raw thermal diffusivity measurements into the desired thermal conductivity data, a formula must be applied requiring the density of the material and the specific heat capacity (Equation 3.3). The density is determined using the material's weight and volume measurements as discussed in Chapter 3, leaving only the material's specific heat capacity. This value can be estimated using the empirical formula given by Equation 3.5.

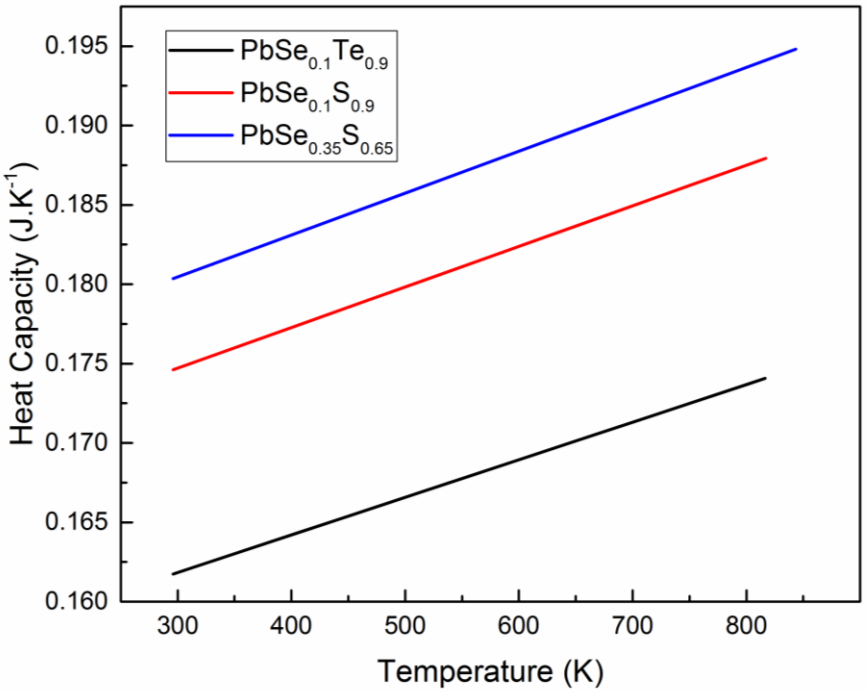

Figure 5.4: The temperature dependent Specific Heat Capacities calculated for $PbSe_{0.1}Te_{0.9}$, $PbSe_{0.1}S_{0.9}$ and $PbSe_{0.35}S_{0.65}$.

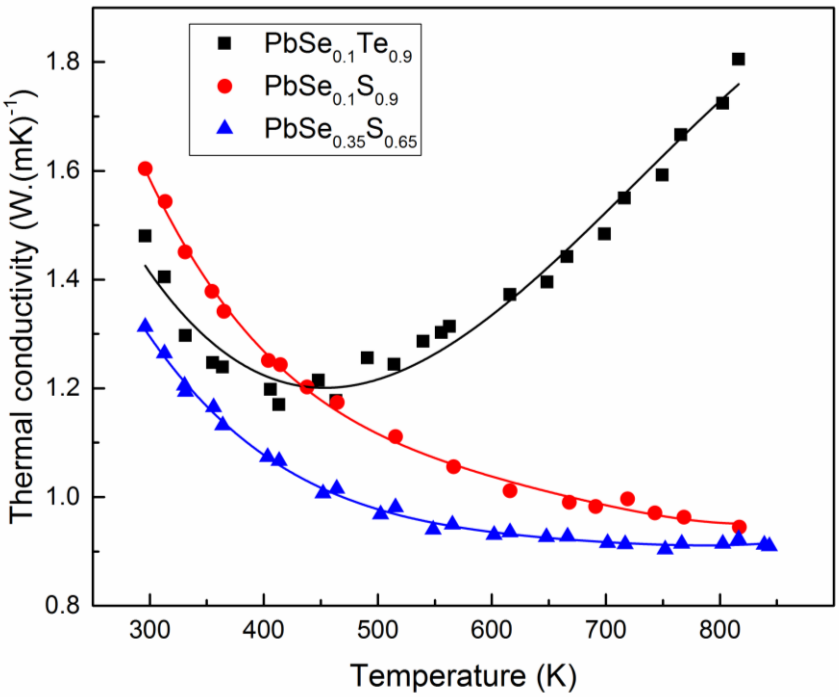

Figure 5.5: The calculated total thermal conductivity for $PbSe_{0.1}Te_{0.9}$, $PbSe_{0.1}S_{0.9}$ and $PbSe_{0.35}S_{0.65}$.

The vast majority of thermoelectric semiconductors possess small band gap energy (<0.5 eV) in comparison to other categories of semiconductors, hence strong bipolar effects begin to influence their properties at high temperature [9, 30, 31]. The bipolar effect is named as such due to the involvement of both holes and electrons in their operation. This effect becomes prevalent in semiconductors when the minority carriers increase in population, achieving similar conductivities to the majority carriers. The identification of the minority and majority carriers relates directly to how each specific semiconductor is doped; holes are the majority charge carriers for p-type semiconductors and electrons are the minority charge carriers. However for n-type semiconductors, electrons are the majority carriers and holes are the minority carriers. Due to the opposing signs of the two charge carriers present, the magnitude of the Seebeck coefficient (|S|), also known as the temperature dependent thermopower, rapidly rises and peaks followed by a sharp decline. Simultaneously the electrical conductivity and thermal conductivity (electronic contribution) depreciate quickly due to phonon scattering to around the same temperature before increasing due to bipolar effects [78].

The Seebeck coefficient doesn't reveal the bipolar effect to the same extent as thermal conductivity [15]. The bipolar effect is much more evident in the thermal conductivity measurements because it is affected by increasing electrical conductivity (κ_e) due to resistivity reduction and significant enhancement of the thermal conductivity bipolar term (κ_b). This bipolar phenomenon is clearly evident in sample $PbSe_{0.1}Te_{0.9}$ shown in Figure 5.5 by the sudden increasing of thermal conductivity when the temperature reaches approximately 400 K. This temperature is where the bipolar effect begins to occur. Figure 5.5 shows lower magnitude of bipolar effect for both samples $PbSe_{0.1}S_{0.9}$ and $PbSe_{0.35}S_{0.65}$ demonstrating flattened regions of thermal conductivities above ~ 600K. The signified bipolar effect in sample $PbSe_{0.1}Te_{0.9}$ is associated to the narrower band gap energy of 0.29 eV for $PbSe_{0.1}Te_{0.9}$ compared to 0.408 and 0.375 eV for $PbSe_{0.1}S_{0.9}$ and $PbSe_{0.35}S_{0.65}$ respectively. For sample $PbSe_{0.1}Te_{0.9}$ only a small amount of thermal energy is required for electrons to jump from the valence band to the conduction band.

The increased band gap in $PbSe_{0.1}S_{0.9}$ and $PbSe_{0.35}S_{0.65}$ samples is predominantly due to the alloying of PbSe with higher band gap compound of PbS and bowing parameters described in Chapter 4. The electronic transport properties of intrinsic ternary PbS-PbSe system has been investigated previously [31]. The samples of the analogue compositions have produced very similar thermal conductivity and room temperature electrical resistivity values to the current study [31]. The intrinsic carrier concentrations of roughly -2.5x10^{18} to -3.0x10^{18} cm^{-3} have been measured for samples over an entire composition range. Similar to the current study, ternary PbSe-PbS alloys show n-type semiconductors.

The room temperature Seebeck coefficients for $PbSe_{0.1}S_{0.9}$ and $PbSe_{0.3}S_{0.7}$ in previous study [31] are -249 and -214 $\mu.V.K^{-1}$ respectively, which is relatively close to measured Seebeck coefficient values of -233 and -201 $\mu.V.K^{-1}$ for $PbSe_{0.1}S_{0.9}$ and $PbSe_{0.35}S_{0.65}$ in the current study. The room temperature electrical resistivities of previous study [31] for $PbSe_{0.1}S_{0.9}$ and $PbSe_{0.3}S_{0.7}$ samples were 4.83 and 3.52 mΩ.cm, slightly lower than 6 and 5 mΩ.cm for $PbSe_{0.1}S_{0.9}$ and $PbSe_{0.35}S_{0.65}$ in the current study. The current study shows the room temperature thermal conductivity of $PbSe_{0.1}S_{0.9}$ and $PbSe_{0.35}S_{0.65}$ to be 1.6 and 1.3 $W.m^{-1}.K^{-1}$, with the previous study recording values marginally higher at 1.9 and 1.4 $W.m^{-1}.K^{-1}$ for $PbSe_{0.1}S_{0.9}$ and $PbSe_{0.3}S_{0.7}$. The room temperature electronic transport properties of current study samples are very close to the similar previous study. Hence, one would assume that samples of both studies possess similar carrier concentrations.

The bipolar effect in narrow band gap semiconductors is influenced significantly by the energy of band gap and carrier concentrations [79]. The larger the samples band gap, the more energy is required to excite the electrons (n-type) or holes (p-type) from the valence band to the conduction band. Hence, if the material has low band gap energy then bipolar conduction will occur at a lower temperature. The carrier concentration of a semiconductor is the other possibility of inducing the bipolar effect. This happens due to intrinsic defects and impurities that are produced during the sample preparation, leading to phonon scattering and an increased carrier concentration. This property can be measured to determine the level of intrinsic doping in each sample,

which will provide a clarification as to which factor has led to the appearance of bipolar conduction in $PbSe_{0.1}Te_{0.9}$.

The large room temperature Seebeck coefficient and electrical resistivity values for the samples in Table 5.1 correspond to very low charge carrier concentrations of these samples originated from intrinsic point defects. Therefore the low temperature upturn in thermal conductivity values of $PbSe_{0.1}Te_{0.9}$ sample is most likely to be associated with small band gap of 0.29 eV for this sample compared to 0.408 eV and 0.375 eV for samples $PbSe_{0.1}S_{0.9}$ and $PbSe_{0.35}S_{0.65}$ respectively. If however the carrier concentration was determined to be higher, the low temperature bipolar effect observed could possibly have been due to intrinsic doping and not completely dependent on the size of the band gap. A high carrier concentration could also have led to increased band gap values for these samples, due to the Burstein-Moss shift that occurs in doped semiconductors [15].

These results confirm the accuracy of measured band gap values in Chapter 4. This also indicates that the bowing observed in band gap energy of ternary and quaternary Pb chalcogenides is originated from atomic interaction of alloying elements with the host elements and the charge carriers have negligible effect on the apparent optical energy of band gaps measured by using FTIR technique.

5.3. Obtaining band gap from temperature Dependent Seebeck and Resistivity

The Seebeck coefficient and electrical resistivity as a function of temperature can also be used to estimate the band gap energy of lead chalcogenide alloys. This method is briefly introduced in Chapter 3 and will be further discussed here.

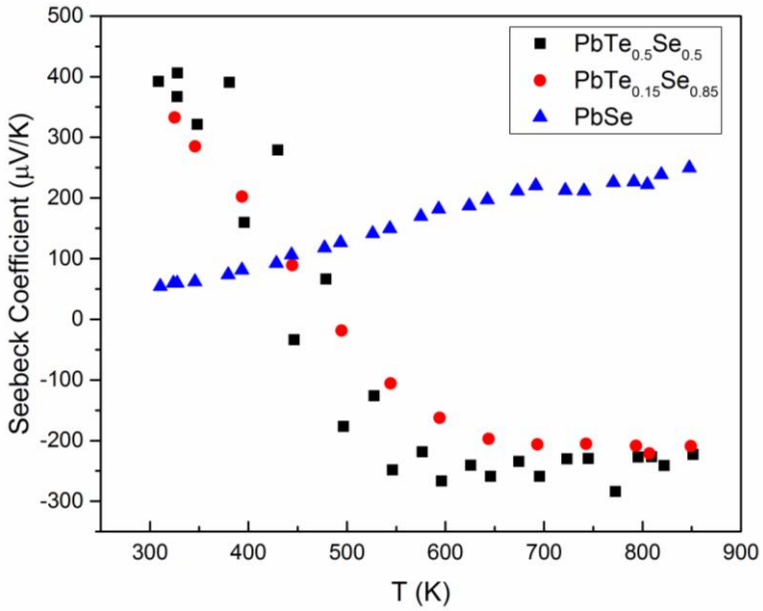

Figure 5.6: The temperature dependent Seebeck coefficient for $PbTe_{0.5}Se_{0.5}$, $PbTe_{0.15}Se_{0.85}$ and PbSe.

In order to obtain the band gap energy using Equation 3.6, ($E_g = 2e|S|_{max}T_{max}$), the maximum Seebeck coefficient ($|S|_{max}$) of each sample must be first determined. Figure 5.6 shows the Seebeck coefficient of samples as a function of temperature obtained from Linsies – Seebeck Coefficient and Electric Resistivity Unit (LSR). The maximum Seebeck value is identified and estimated band gap energy of samples are summarized in Table 5.2.

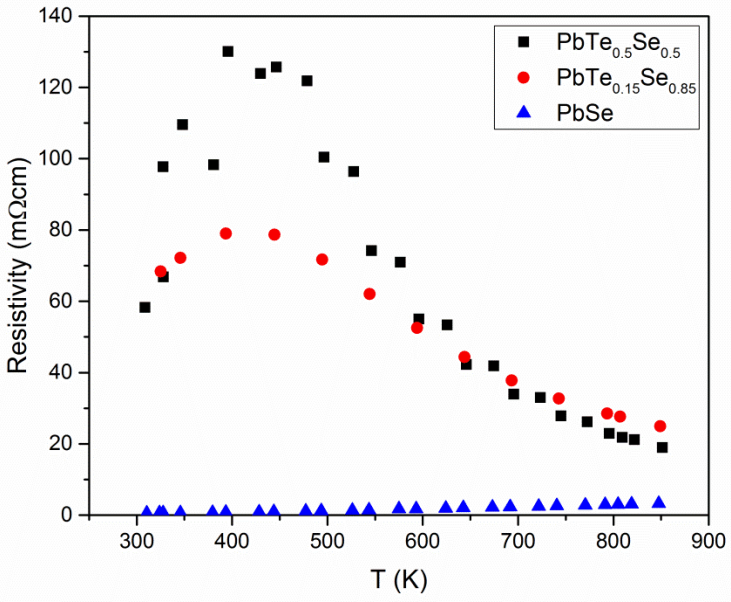

Figure 5.7: The measured electrical resistivity as a function of temperature for $PbTe_{0.5}Se_{0.5}$, $PbTe_{0.15}Se_{0.85}$ and PbSe.

Equation 3.7, ($\rho(T) = \rho_0 exp\left(-\frac{E_g}{2k_BT}\right)$), is also used to estimate the band gap energy of semiconductors [25]. Figure 5.7 shows the electrical resistivity of samples in Figures 5.6 as a function of temperature. The energy gap (Eg) in Equation 3.7 is determined from the slope of the line in Figure 5.8, where the natural logarithmic function (ln) of resistivity is plotted versus the inverted temperature (1/T). It is evident that the PbSe sample is positioned well below the other samples and decreases with inverse temperature. As mentioned in Chapter 3 this technique is only valid for intrinsic semiconductors and it is obvious in Figure 5.7 from the steady increase in resistivity with temperature this indicates a doped semiconductors. Hence, the estimated band gap calculated from this data is negligible and will not produce an accurate result. These results are summarized in Table 5.2.

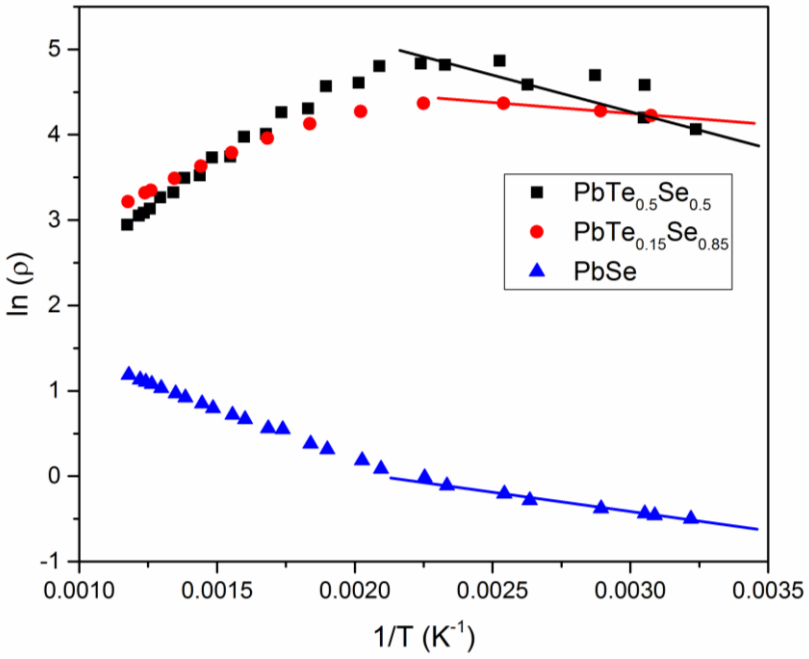

Figure 5.8: The estimated band gap energies for $PbTe_{0.5}Se_{0.5}$, $PbTe_{0.15}Se_{0.85}$ and PbSe.

Table 5.2: The calculated band gap energies for $PbTe_{0.5}Se_{0.5}$, $PbTe_{0.15}Se_{0.85}$ and PbSe using the temperature dependent Seebeck and resistivity.

Sample	Band Gap (eV) from Seebeck	Band Gap (eV) from Resistivity	Band Gap (eV) from Optical Measurements
PbTe0.5Se0.5	0.266	0.146	0.299
PbTe0.15Se0.85	0.216	0.046	0.280
PbSe	0.422	0.075	0.270

Table 5.2 summarizes the band gap energies obtained for $PbTe_{0.5}Se_{0.5}$, $PbTe_{0.15}Se_{0.85}$ and PbSe samples from direct optical band gap measurement (described in Chapter 4) and estimated energy gaps from temperature dependent Seebeck and resistivity data. Clearly, the estimated energy gaps are different from measured optical measurements in Chapter 4. The estimated values of energy gaps in Table 5.2 appear to randomly change as a function of composition, opposed to Figure 4.5 which shows a parabolic relation of measured energy gaps with PbSe concentration.

This discrepancy between optical and electronic property measurements has been identified previously [15], where it was concluded that the optical measurements were more accurate with less error ($\pm$ 0.04 < $\pm$ 0.10 eV). The large error appears on the estimation of the band gap from temperature dependent resistivity is shown to be originated from the assumption that the sample is a perfect intrinsic semiconductor containing a number of holes and electrons with equal mobility. However, the mobility of holes and electrons in lead chalcogenide alloy is never equal [80] therefore, the accuracy of these estimations is significantly reduced. Similarly, the minority carriers in each sample heavily affect the maximum Seebeck coefficient recorded in Figure 5.6 and rely on the principal of equal mobility in holes and electrons.

Chapter 6

6.1. Conclusion

The band gap energies of ternary $(PbTe)_{1-x}(PbSe)_x$ and quaternary $(PbTe)_{0.9-y}(PbSe)_{0.1}(PbS)_y$ and $(PbTe)_{0.65-y}(PbSe)_{0.35}(PbS)_y$ systems were measured to determine their changes with composition. It is revealed that the band gap energy produced a positive bowing over the range of compositions. This has challenged the well-accepted linear projection of composition dependent band gap energies for solid solution lead chalcogenide alloys. An attempt was made to rationalise the bowing phenomenon in these systems and investigate the factors affecting its magnitude. These factors include ionicity mismatch, crystal lattice mismatch, solubility, valence electron potential and electronegativity.

The ternary $(PbTe)_{1-x}(PbSe)_x$ system produced a small band gap bowing of -0.052 ± 0.011 eV, predominantly due to the difference in valence electron potential and electronegativity. The results have shown an increased bowing parameter for the quaternary systems containing PbS of -0.21813 ± 0.01561 and -0.08326 ± 0.02352 eV for $(PbTe)_{0.9-y}(PbSe)_{0.1}(PbS)_y$ and $(PbTe)_{0.65-y}(PbSe)_{0.35}(PbS)_y$ respectively, due to the larger ionicity and crystal lattice mismatch. Of the two quaternary systems containing PbS, $(PbTe)_{0.9-y}(PbSe)_{0.1}(PbS)_y$ returned a higher bowing parameter than $(PbTe)_{0.65-y}(PbSe)_{0.35}(PbS)_y$ primarily due to its larger miscibility gap.

The temperature dependent thermal conductivities were also measured for $PbSe_{0.1}Te_{0.9}$, $PbSe_{0.1}S_{0.9}$ and $PbSe_{0.35}S_{0.65}$ samples. The results revealed the presence of larger degree bipolar conduction at lower temperature for the PbS-free $PbSe_{0.1}Te_{0.9}$ compound than the other two alloys. The bipolar effect in the semiconductors occurs due to narrow band gap width or increased carrier concentration, which results in Burstein Moss shift. The large room temperature electrical resistivity and Seebeck coefficient of these samples suggested minimal contribution from intrinsic defect

charge carrier effect. Therefore it is concluded that larger band gaps of 0.408 and 0.375 eV for $PbSe_{0.1}S_{0.9}$ and $PbSe_{0.35}S_{0.65}$ samples respectively compared to 0.29 eV for PbS-free sample of $PbSe_{0.1}Te_{0.9}$ has reduced the contribution of thermally activated minority charge carrier in conductivity.

The electronic band gap estimations for a small number of samples were calculated using temperature dependent Seebeck and resistivity measurements. This was undertaken in order to explore the accuracy of this type of result and compare this data with the optical band gap measurements. As predicted from previous research these results did not agree, however they were within the error for electronic band gap estimations (± 0.1 eV).

6.2. Future Work

There are a number of future projects that could be researched as a continuation of my thesis findings. Maintaining the compositions used here of ternary $(PbTe)_{1-x}(PbSe)_x$ and quaternary $(PbTe)_{0.9-y}(PbSe)_{0.1}(PbS)_y$ and $(PbTe)_{0.65-y}(PbSe)_{0.35}(PbS)_y$, the effects on the band gap values at higher temperatures could be further explored.

This would involve an investigation into band convergence of lead chalcogenide alloys at increased temperatures. The data obtained could then be analysed and graphed as a function of composition to determine whether it follows a similar trend to the room temperature graph i.e. band gap bowing occurs.

References

1. Volykhov, A.A., L.V. Yashina, and V.I. Shtanov, *Phase relations in pseudobinary systems of germanium, tin, and lead chalcogenides.* Inorganic Materials, 2006. **42**(6): p. 596-604.
2. Zhao, L., *Investigation on the electronic structures, hardness and thermoelectric properties of superionic thermoelectric materials.* 2016.
3. Ravich, Y.I., *Monographs in Semiconductor Physics*. Semiconducting Lead Chalcogenides, ed. L.S. Stil'bans. Vol. 5. 1970, New York: Plenum Press. 377.
4. Scanlon, W.W., *Recent advances in the optical and electronic properties of PbS, PbSe, PbTe and their alloys.* Journal of Physics and Chemistry of Solids, 1959. **8**(0): p. 423-428.
5. Cowley, R.A., *On the theory of ferroelectricity and anharmonic effects in crystals.* Philosophical Magazine, 1965. **11**(112): p. 673-706.
6. Gibbs, Z.M., et al., *Temperature dependent band gap in PbX (X = S, Se, Te).* Applied Physics Letters, 2013. **103**(26): p. 262109.
7. Chaudhuri, T.K., *A solar thermophotovoltaic converter using Pbs photovoltaic cells.* International Journal of Energy Research, 1992. **16**(6): p. 481-487.
8. Aminorroaya, S., et al., *Thermoelectric Properties and Microstructure Studies of Spinodally Decomposed PbTe0. 38S0. 62 Alloy.* Science of Advanced Materials, 2014. **6**(7): p. 1453-1459.
9. Aminorroaya Yamini, S., et al., *Thermoelectric Performance of n-Type (PbTe) 0.75 (PbS) 0.15 (PbSe) 0.1 Composites.* ACS applied materials & interfaces, 2014. **6**(14): p. 11476-11483.
10. Yamini, S.A., et al., *Thermoelectric performance of tellurium-reduced quaternary p-type lead–chalcogenide composites.* Acta Materialia, 2014. **80**: p. 365-372.
11. LaLonde, A.D., et al., *Lead telluride alloy thermoelectrics.* Materials Today, 2011. **14**(11): p. 526-532.
12. Ekuma, C.E., et al., *Optical properties of PbTe and PbSe.* Physical Review B, 2012. **85**(8): p. 085205.
13. Pei, Y., et al., *Convergence of electronic bands for high performance bulk thermoelectrics.* Nature, 2011. **473**(7345): p. 66-9.
14. Pei, Y., H. Wang, and G.J. Snyder, *Band Engineering of Thermoelectric Materials.* Advanced Materials, 2012. **24**(46): p. 6125-6135.
15. Gibbs, Z.M., A. LaLonde, and G.J. Snyder, *Optical band gap and the Burstein–Moss effect in iodine doped PbTe using diffuse reflectance infrared Fourier transform spectroscopy.* New Journal of Physics, 2013. **15**(7): p. 075020.
16. Ahn, S., et al., *Determination of band gap energy (Eg) of Cu2ZnSnSe4 thin films: On the discrepancies of reported band gap values.* Appl. Phys. Lett, 2010. **97**(2): p. 021905.
17. Volykhov, A., L. Yashina, and V. Shtanov, *Phase equilibria in pseudoternary systems of IV–VI compounds.* Inorganic Materials, 2010. **46**(5): p. 464-471.
18. Pei, Y., et al., *Stabilizing the Optimal Carrier Concentration for High Thermoelectric Efficiency.* Advanced Materials, 2011. **23**(47): p. 5674-5678.

19. Crocker, A. and L. Rogers, *Valence band structure of PbTe.* Le Journal de Physique Colloques, 1968. **29**(C4): p. C4-129-C4-132.
20. May, A.F., et al., *Characterization and analysis of thermoelectric transport in n-type $Ba_8Ga_{16-x}Ge_{30+x}$.* Physical Review B, 2009. **80**(12): p. 125205.
21. Wang, H., et al., *Tuning bands of PbSe for better thermoelectric efficiency.* Energy & Environmental Science, 2014. **7**(2): p. 804-811.
22. Tauber, R., A. Machonis, and I. Cadoff, *Thermal and optical energy gaps in PbTe.* Journal of Applied Physics, 1966. **37**(13): p. 4855-4860.
23. Aminorroaya Yamini, S., et al., *Chemical composition tuning in quaternary p-type Pb-chalcogenides - A promising strategy for enhanced thermoelectric performance.* Physical Chemistry Chemical Physics, 2014. **16**(5): p. 1835-1840.
24. Jaworski, C.M., et al., *Valence-band structure of highly efficient p-type thermoelectric PbTe-PbS alloys.* Physical Review B, 2013. **87**(4): p. 045203.
25. Gibbs, Z.M., *Band Engineering in Thermoelectric Materials Using Optical, Electronic, and Ab-Initio Computed Properties*. 2015, California Institute of Technology.
26. Zhao, J., et al., *Spectroscopic evidence for the convergence of lower and upper valence bands of PbQ (Q=Te, Se, S) with rising temperature.* 2014.
27. Drabkin, I., *Fundamental absorption edge of heavily doped n-type PbTe.* Soviet Physics-Semiconductors, 1975. **8**(7): p. 900.
28. Zhao, L.D., et al., *High thermoelectric performance via hierarchical compositionally alloyed nanostructures.* J Am Chem Soc, 2013. **135**(19): p. 7364-70.
29. Korkosz, R.J., et al., *High ZT in p-type (PbTe)1-2x(PbSe)x(PbS)x thermoelectric materials.* J Am Chem Soc, 2014. **136**(8): p. 3225-37.
30. Pei, Y., et al., *High thermoelectric figure of merit in heavy hole dominated PbTe.* Energy & Environmental Science, 2011. **4**(6): p. 2085-2089.
31. Wang, J.L., et al., *Characteristics of lattice thermal conductivity and carrier mobility of undoped PbSe-PbS solid solutions.* Journal of Physics D: Applied Physics, 2013. **46**(40): p. 405301.
32. Goldsmid, H.J., *Thermoelectric refrigeration*. 1964, New York: Plenum Press.
33. Mahan, G., *Solid State Physics, 51, eds. H. Ehrenreich and F. Spaepen*. 1998, Academic Press.
34. Goldsmid, H.J., *Introduction to thermoelectricity*. Vol. 121. 2010: Springer.
35. Crocker, A. and B. Sealy, *Some physical properties of the PbTe-MgTe alloy system.* Journal of Physics and Chemistry of Solids, 1972. **33**(12): p. 2183-2190.
36. Rogers, L. and A. Crocker, *Transport and optical properties of the MgxPb1− x Te alloy system.* Journal of Physics D: Applied Physics, 1971. **4**(7): p. 1016.
37. Nikolic, P., *Solid solutions of CdSe and CdTe in PbTe and their optical properties.* British Journal of Applied Physics, 1966. **17**(3): p. 341.
38. Wirths, S., et al., *Band engineering and growth of tensile strained Ge/(Si) GeSn heterostructures for tunnel field effect transistors.* Applied physics letters, 2013. **102**(19): p. 192103.
39. Broderick, C.A., et al., *Band engineering in dilute nitride and bismide semiconductor lasers.* Semiconductor Science and Technology, 2012. **27**(9): p. 094011.

40. Atsushi Yamaguchi, A., *Valence band engineering for remarkable enhancement of surface emission in AlGaN deep ‐ ultraviolet light emitting diodes.* physica status solidi (c), 2008. **5**(6): p. 2364-2366.
41. Rouraa, P., et al., *Determination of the direct band-gap energy of InAlAs matched to InP by photoluminescence excitation spectroscopy.* Strain, 1997. **10**: p. 3.
42. Tauc, J., *Optical properties and electronic structure of amorphous Ge and Si.* Materials Research Bulletin, 1968. **3**(1): p. 37-46.
43. Planck, M., *On the law of distribution of energy in the normal spectrum.* Annalen der Physik, 1901. **4**(553): p. 1.
44. Urbach, F., *The Long-Wavelength Edge of Photographic Sensitivity and of the Electronic Absorption of Solids.* Physical Review, 1953. **92**(5): p. 1324-1324.
45. Pankove, J.I., *Absorption Edge of Impure Gallium Arsenide.* Physical Review, 1965. **140**(6A): p. A2059-A2065.
46. Kubelka, P., *Phys. 1931, 12, 593–601; b) P. Kubelka.* Journal of the Optical Society of America. A, Optics and image science, 1948. **38**(44): p. 8.
47. Hecht, E. and A. Zajac, *Optics, fourth printing*. 1974, Addison-Wesley Publishing Company, Reading, MA.
48. Suárez, M., et al., *Challenges and opportunities for spark plasma sintering: a key technology for a new generation of materials*. 2013: INTECH Open Access Publisher.
49. Boroumand, F., J.E. Moser, and H. van den Bergh, *Quantitative Diffuse Reflectance and Transmittance Infrared Spectroscopy of Nondiluted Powders.* Applied Spectroscopy, 1992. **46**(12): p. 1874-1886.
50. Cowan, R.D., *Pulse method of measuring thermal diffusivity at high temperatures.* Journal of Applied Physics, 1963. **34**(4): p. 926-927.
51. Pashinkin, A.S., et al., *Heat capacity and thermodynamic properties of lead selenide and lead telluride.* Inorganic Materials, 2009. **45**(11): p. 1226-1229.
52. Goldsmid, H.J. and J.W. Sharp, *Estimation of the thermal band gap of a semiconductor from seebeck measurements.* Journal of Electronic Materials, 1999. **28**(7): p. 869-872.
53. Akhtar, J., et al., *Controlled Synthesis of Tuned Bandgap Nanodimensional Alloys of PbSxSe1−x.* Journal of the American Chemical Society, 2011. **133**(14): p. 5602-5609.
54. Korkosz, R.J., et al., *High ZT in p-Type (PbTe)1–2x(PbSe)x(PbS)x Thermoelectric Materials.* Journal of the American Chemical Society, 2014. **136**(8): p. 3225-3237.
55. Pei, Y., et al., *Convergence of electronic bands for high performance bulk thermoelectrics.* Nature, 2011. **473**(7345): p. 66-69.
56. Aminorroaya Yamini, S., et al., *High thermoelectric performance of Tellurium-reduced quaternary p-type lead-chalcogenide composites.* Acta Materialia, 2014. **80**: p. 365-372.
57. Lee, S., et al., *Band-gap nonlinearity in perovskite structured solid solutions.* Journal of Applied Physics, 2010. **107**(2): p. 023523.
58. Berrah, S., A. Boukortt, and H. Abid, *The composition effect on the bowing parameter in the cubic InGaN, AlGaN and AlInN alloys.* 2008. **11**(1): p. 59-62.

59. Tit, N., I.M. Obaidat, and H. Alawadhi, *Origins of bandgap bowing in compound-semiconductor common-cation ternary alloys.* Journal of Physics: Condensed Matter, 2009. **21**(7): p. 075802.
60. Shimakawa, K., *On the compositional dependence of the optical gap in amorphous semiconducting alloys.* Journal of Non-Crystalline Solids, 1981. **43**(2): p. 229-244.
61. Shi, H.L. and Y. Duan, *Band-gap bowing and p-type doping of (Zn, Mg, Be)O wide-gap semiconductor alloys: a first-principles study.* The European Physical Journal B, 2008. **66**(4): p. 439-444.
62. Boukhris, N., et al., *Ab initio study of the structural, electronic and thermodynamic properties of PbSe 1− x S x , PbSe 1− x Te x and PbS 1− x Te x ternary alloys.* Physica Scripta, 2011. **83**(6): p. 065701.
63. Rockett, A., *The Materials Science of Semiconductors*. 2010, New York: Springer Science+ Business Media.
64. Doak, J.W. and C. Wolverton, *Coherent and incoherent phase stabilities of thermoelectric rocksalt IV-VI semiconductor alloys.* Physical Review B, 2012. **86**(14): p. 144202.
65. Van Vechten, J.A. and T.K. Bergstresser, *Electronic Structures of Semiconductor Alloys.* Physical Review B, 1970. **1**(8): p. 3351-3358.
66. Charifi, Z., H. Baaziz, and N. Bouarissa, *ENERGY BAND-GAPS OF Mg x Zn 1-x Se: VIOLATION OF VEGARD'S LAW.* International Journal of Modern Physics B, 2004. **18**(01): p. 137-142.
67. Phillips, J.C. and L. Kleinman, *New method for calculating wave functions in crystals and molecules.* Physical Review, 1959. **116**(2): p. 287.
68. Shannon, R.t., *Revised effective ionic radii and systematic studies of interatomic distances in halides and chalcogenides.* Acta Crystallographica Section A: Crystal Physics, Diffraction, Theoretical and General Crystallography, 1976. **32**(5): p. 751-767.
69. Pauling, L., *The chemical bond: a brief introduction to modern structural chemistry*. 1967: Cornell University Press.
70. Volykhov, A., L. Yashina, and V. Shtanov, *Phase relations in pseudobinary systems of germanium, tin, and lead chalcogenides.* Inorganic Materials, 2006. **42**(6): p. 596-604.
71. Girard, S.N., et al., *Analysis of Phase Separation in High Performance PbTe–PbS Thermoelectric Materials.* Advanced Functional Materials, 2012. **23**(6): p. 747-757.
72. Aminorroaya Yamini, S., et al., *Heterogeneous distribution of sodium for high thermoelectric performance of p-type multiphase lead-chalcogenides.* Advanced Energy Materials, 2015. **5**(21): p. 1501047.
73. LaLonde, A.D., Y. Pei, and G.J. Snyder, *Reevaluation of PbTe1-xIx as high performance n-type thermoelectric material.* Energy & Environmental Science, 2011. **4**(6): p. 2090-2096.
74. Wang, H., et al., *Thermoelectric alloys between PbSe and PbS with effective thermal conductivity reduction and high figure of merit.* Journal of Materials Chemistry A, 2014. **2**(9): p. 3169-3174.
75. Wang, H., et al., *High Thermoelectric Efficiency of n-type PbS.* Advanced Energy Materials, 2012. **3**(4): p. 488-495.

76. Wang, H., et al., *Weak electron-phonon coupling contributing to high thermoelectric performance in n-type PbSe.* Proceedings of the National Academy of Sciences of the United State of America, 2012. **109**(25): p. 9705-9.
77. Aminorroaya Yamini, S., et al., *Thermoelectric performance of n-type $PbSe_{0.1}S_{0.15}Te_{0.75}$ composites.* ACS Applied Materials & Interfaces, 2014. **6**(14): p. 11476-11483.
78. LaLonde, A.D., Y. Pei, and G.J. Snyder, *Reevaluation of PbTe 1− x I x as high performance n-type thermoelectric material.* Energy & Environmental Science, 2011. **4**(6): p. 2090-2096.
79. Gong, J., et al., *Investigation of the bipolar effect in the thermoelectric material CaMg 2 Bi 2 using a first-principles study.* Physical Chemistry Chemical Physics, 2016.
80. Ravich, Y.I., B.A. Efimova, and I.A. Smirnov, *Semiconducting lead chalcogenides* 1970: Plenum Press in New York.